Renewable resources derived hyperbranched polyurethane/ oxygeneous-graphitic carbon nitride dots nanocomposite

Highlight

The current chapter describes the formation of nanocomposite of renewable resource derived hyperbranched polyurethane (HPU) with oxygeneous-graphitic-carbon nitride dot (oxy-g-CND). Fabrication of the nanocomposite was achieved by an *in situ* polymerization technique using four different loadings (0.5, 1.0, 2.0 and 3.0 wt%) of the nanodot. The oxy-g-CND and fabricated nanocomposites were characterized by various spectroscopic, microscopic and analytical techniques. The processed nanocomposite demonstrated improved physico-mechanical properties *viz*. tensile strength (upto 1.9 fold), elongation at break (upto 1.2 fold) and toughness (upto 2.5 fold) as well as enhanced thermal stability (above 310 °C) than the pristine HPU. The nanocomposite displayed remarkable photoluminescent property in solvent-dispersed state. The nanocomposite was consequently employed as an UV light-detectable anti-counterfeiting ink material. Further, the nanocomposite film with higher loading of oxy-g-CND was utilized as a solar light-assisted heterogeneous metal-free photocatalyst towards oxidation and reduction reactions.

Excerpts of this chapter are published/communicated in:

[1] **Bayan, R.** and Karak, N. Photoluminescent oxygeneous-graphitic carbon nitride nanodots incorporated bio-derived hyperbranched polyurethane nanocomposite with anti-counterfeiting attribute, *ACS Omega*, 4(5):9219-9227, 2019.

[2] **Bayan, R.** and Karak, N. Bio-based hyperbranched polymer-supported oxygeneous graphitic-carbon nitride dot as heterogeneous metal-free solar light photocatalyst for oxidation and reduction reactions, *Applied Surface Science*, 514:145909, 2020.

6.1.   Introduction

As discussed in the previous chapters, carbon based nanomaterials with their myriad properties have carved out a niche for themselves that can be exploited to build polymeric nanocomposites for various applications. In this context, graphitic carbon nitride is a new emerging nanomaterial that has attracted considerable interest in recent years, due to its similarity to graphene [1]. Graphitic carbon nitride consists of a pre-bonded C-N core motif that imparts unique features viz. thermal stability, chemical stability, optical property, electrochemical property, surface property, etc [1, 2]. Variants of graphitic carbon nitride in the form of nanosheets and nanodots have found widespread applications as photocatalysts, electrochemical sensors, energy storage devices, environmental remediators, etc [2-5]. From this perspective, graphitic carbon nitride due to their uncanny structural similarity to graphene can be thereby utilized as nano-reinforcing agent for improving the properties of polymers. However, till date, there have been very few reports on their use in polymer nanocomposite. For instance, Zhu et al. reported the development of graphitic carbon nitride nanosheets-reinforced polyimide nanocomposite with enhanced mechanical and tribological properties [6]. Xu et. al. demonstrated graphitic carbon nitride nanosheets-reinforced poly(urea-urethane) nanocomposite with self healing and anti-corrosive properties [7]. Thus, there is plenty of scope for graphitic carbon nitride with its unique structural features and attractive set of properties to be applied as reinforcing materials for polymer nanocomposites.

Again, in the current times, counterfeiting has become a rising issue worldwide for industries, governments and customers. With the recent development and generalization of high-end equipments, counterfeited items have become more common, creating problem for the society [8]. For example, the circulation of counterfeited paper currency leads to serious socio-economic problems as well as undervalue authentic currency [9, 10]; production and distribution of counterfeited drugs poses severe health hazard, as they may contain unknown or incorrect amount of chemicals [11, 12]. In this context, anti-counterfeiting has become a vital innovation for protection of essential and valuable items from duplication such as currency, documents, certificates, products, trademarks, luxury items and tickets [8]. During the past decade, an array of anti-counterfeiting technologies has been developed to tackle counterfeiting. However, the counterfeiters have been successful in adapting to the current methods, which makes it imperative to develop new materials and innovative tools to detect and prevent counterfeiting. In this perspective, functional materials having distinct physical, chemical or optical properties can be expected to provide anti-counterfeiting measures, due to difficulties associated with reproduction of

their unique functions [13]. Especially, photoluminescent materials with specific-excitation and specific-mode emission properties are considered to be good strategy for anti-counterfeiting applications [14, 15]. In this context, graphitic carbon nitride nanodots, with their excellent optical and photoluminescent properties, can serve as an ideal material for constructing anti-counterfeiting material that shows specific-excitation/emission properties. These photoluminescent nanodots combined with the unique attributes of bio-based HPUs can forge a suitable material that is not only robust and eco-friendly, but also intricate in its design. The design of such high performance photoluminescent nanocomposites can be a prototype for coatings, labeling, ink-jet printing with anti-counterfeiting measures.

Again, photocatalysis is considered to be an energy-conservative, inexpensive and green technique for driving various organic transformations [16]. Utilization of light energy for promoting organic transformations has seen an enormous interest over the last decade for its clean and environmental friendly attributes. In this milieu, solar light or sunlight – the universal source of light is considered to be a prime source of renewable energy, consisting of about 5% of UV light, 50% of visible light and 45% of infrared light at the surface of the earth. Harnessing such form of renewable energy for promoting organic transformations is likely the key to develop clean and green alternative to the conventional and advanced techniques like heating, microwave, ultrasound, etc [17]. Based on this idea, many potential photocatalysts have been designed to exploit the power of solar energy. However, most of these photocatalysts involve metal-based systems or intricately designed complexes/compounds that include TiO_2, ZnO, Fe_2O_3, CdS, Bi_2WO_6, $BiVO_4$, Ta_2O_5, Ta_3N_5, $TaON$, and many more, which do not completely adhere to the tenets of green chemistry [3]. Therefore, development of novel, metal-free solar light-harvesting photocatalytic systems has been gaining copious amount of attention in the recent times. In this regard, graphitic-carbon nitride (g-CN) is quickly emerging as neo-generation material for developing green and efficient solar light-harvesting photocatalytic systems. Layer-structured metal-free g-CN opened up a new class of polymeric photocatalysts, due to its high thermostability, chemical stability, low cost and facile preparation and most importantly, suitable band structure [4, 5]. Moreover, its optical and electronic properties can be tuned by implanting heteroatoms and vacancy defects into its near-graphitic domains that ensure effective charge carrier separation to enhance photocatalytic activity, especially in the UV-visible region [18-20]. This allows its direct use in sustainable chemistry as a promising heterogeneous metal-free photocatalyst, for example, hydrogen evolution [18, 19], water-splitting [20], and organic transformations of hydrocarbons [21-28]. However, the practical problem associated with g-CN in photocatalytic process, stems

from its high dispersibility in water (nano-level) and sometimes alcohols, which may give rise to tedious isolation process. In this regard, the application of a polymeric material may provide a suitable rigid support to promote the photocatalytic activity of g-CN, inhibiting their solid state quenching and benefiting straightforward isolation from reaction medium. In this milieu, hyperbranched polymers and dendrimers are considered to be apt materials, due to their 3-D architectures with internal pores and cavities, large number of surface functionalities, mechanical and thermal stability, etc [29, 30]. The utility of hyperbranched and dendritic polymers in catalysis has been very seldom discussed, although they offer interesting features like cage-like structures with pores and cavities, heterogeneous nature, selectivity of products and easy isolation and recovery [30-32].

Now, speaking about organic transformations, selective oxidation of aromatic alcohols to carbonyls and its reverse reaction, reduction of aromatic carbonyls to alcohols are the most elementary and significant transformations in the realms of organic chemistry, due to their significance as precursors and intermediates in various synthetic protocols, pharmaceutical industries and large-scale production of fine chemicals [33, 34]. Traditional protocols in these transformations involve metals in stoichiometric amounts that are toxic and hazardous, along with harsh reaction conditions and large number of by-products [35, 36]. Therefore, the use of photocatalytic approach provides an alternative methodology to obtain such transformations using a pollution-free energy source. In a bid to approach this issue, g-CN nanodots (g-CNDs) embedded in HPU can be applied as a potential solar-light harvesting material for such photocatalytic reactions. The use of g-CNDs can provide a clean and green energy route. At the same time, the bio-derived HPU can provide an eco-friendly mechanical support system for the photocatalytic activity of g-CNDs and large number of surface functionalities in the polymer matrix, allowing easy activation of the aromatic substrates.

In this perspective, the fabrication of renewable resource derived HPUNC with oxygeneous-g-CND (oxy-g-CND) by *in situ* polymerization was accounted. The influence of the oxygeneous-graphitic carbon nitride nanodots as a nano-reinforcing agent on the mechanical and thermal properties of the nanocomposite was studied. The fabricated nanocomposite was ultimately screened as a high performance material with optical properties. The application of the nanocomposite as an anti-counterfeiting tool was demonstrated. Further, the performance of the nanocomposite as a metal-free heterogeneous solar light driven-photocatalyst in oxidation and reduction reactions of important aromatic compounds was analyzed.

6.2. Experimental

6.2.1. Materials

PCL, IPDI, MGE, COMP and xylene were used for the preparation of HPUNC. All these chemical possess the same grade and specifications as described in Chapter 2 (Section 2.2.1). DMF, of same grade and specifications as mentioned in Chapter 3 (Section 3.2.1) was used in the fabrication of the nanocomposite.

Guanidine hydrochloride was used as a precursor for the preparation of oxygeneous-graphitic-carbon nitride. It is a colorless crystalline compound with molar mass of 95.53 g mol^{-1}, density of 1.35 g cm^{-3} and melting point of 183 °C. It is highly soluble in water and ethanol. Guanidine hydrochloride (98% purity) was obtained from Alfa Aesar, India and used as received.

Sodium citrate dihydrate was used as a precursor for preparation of oxygeneous-graphitic-carbon nitride. It is a colorless crystalline compound with molar mass of 294.10 g mol^{-1}, density of 1.7 g cm^{-3} and melting point > 183 °C. It is highly water soluble and mildly alkaline.

Sodium citrate dihydrate (99% purity) was obtained from SRL, India and used as received. Ammonia solution (liq. NH$_3$), of similar grade and specification as mentioned in Chapter 3 (Section 3.2.1) was used in the preparation of oxygeneous-graphitic-carbon nitride.

Quinine sulfate (Sigma Aldrich, USA) was used as the reference compound for the determination of quantum yield of oxygeneous-graphitic-carbon nitride.

Benzyl alcohol and its derivatives (Merck, India and Alfa Aesar, India), and benzaldehyde and its derivatives (Merck, India; Loba Chemie, India and Alfa Aesar, India) were used as substrates in the photo-catalytic oxidation and reduction reactions. Silica gel G, silica gel GF 254 (SRL, India) and Silica gel 60-120 mesh (SRL, India) of similar specifications and grade, as described in Chapter 5A were utilized for performing TLC and column chromatographic isolation of the crude products. Hydrogen peroxide solution (H$_2$O$_2$, 30% v/v, Merck, India), sodium hypochlorite solution (NaOCl, 4% w/v, Merck, India) and *tert*-butyl hydrogen peroxide (TBHP, 70% v/v, Sigma Aldrich, USA) were used as oxidants in the photo-catalytic oxidation reactions. 2,2,6,6-Tetramethylpiperidin-1-yl)oxyl (TEMPO, 98% purity, Sigma Aldrich, USA) was used as radical scavengers in the photo-catalytic reactions. Other chemicals and solvents used in the catalytic reactions include ethanol, methanol, isopropanol, toluene, chloroform and acetonitrile were of reagent grade and purchased from Merck, India.

6.2.2. Methods

6.2.2.1.   Preparation of oxy-g-CND

Oxy-g-CND was prepared by microwave-assisted pyrolysis technique with slight modification of an earlier report [37]. Briefly, guanidine hydrochloride and sodium citrate dihydrate in the mol ratio of 9:1 were homogenized together in deionized water and pH of the mixture was adjusted to 12 using 25% aqueous NH_3. Subsequently, the reactants were subjected to microwave irradiation for 8 min in a domestic microwave oven, operating at power output of 600 W. After cooling, the as-obtained dark brown residue was dissolved in deionized water and filtered to separate the coarse residue. The filtrate is further centrifuged (at 3000 rpm) to separate any suspended particulates and the light yellow supernatant is collected to give highly water dispersible oxy-g-CNDs (concentration of 22 mg mL^{-1}). Water was removed under reduced pressure and the oxy-g-CND stored in a vaccum desiccator.

6.2.2.2.   Fabrication of HPU/oxy-g-CND nanocomposite

HPU/oxy-g-CND nanocomposite was fabricated by an *in situ* technique, following the same process as described in Chapter 3 (Section 3.2.2.1). Only in this case, a stable dispersion of oxy-g-CND (in DMF) was incorporated in the second step of the polymerization reaction under constant mechanical agitation.

HPU nanocomposites with different weight percentage of oxy-g-CND, *viz.* 0.5 wt%, 1.0 wt%, 2.0 wt% and 3.0 wt% were prepared and encoded as HPUNC0.5, HPUNC1.0, HPUNC2.0 and HPUNC3.0, respectively. In the same way, pristine HPU was prepared for comparison purpose. Pristine HPU is HPU3, as expressed in Chapter 2.

6.2.2.3.   Sample preparation for performance study

Samples of HPUNC compositions were processes in the same way as HPU, as described in Chapter 2 (Section 2.2.2.3). The entire analysis and testing were performed using bulk HPUNC samples without any further purification.

For anti-counterfeiting ink application, dispersions of the HPUNC was prepared in xylene as solvent and used directly as ink material.

For catalytic application, the processed HPUNC thin films were cut into fine pieces and used directly as catalyst.

6.2.2.4.   Quantum yield calculation

The quantum yield of oxy-g-CND was estimated, as per standard procedure by using the following equation [37].

$$\varphi_X = \varphi_R \times \left(\frac{I_X}{I_R}\right) \times \left(\frac{A_R}{A_X}\right) \times \left(\frac{\eta_X^2}{\eta_R^2}\right) \qquad \textbf{(Eq. 6.1)}$$

where φ is the quantum yield, I is the measured integrated emission intensity, A is the optical density, and η is the refractive index. Subscripts X and R refers to the sample and reference standard. Quinine sulfate in 0.1 M H_2SO_4 (literature quantum yield of 0.54 at 360 nm) was used as the reference standard.

6.2.2.5.   Optical band gap calculation

The optical band gap calculation was performed by UV-Vis spectroscopy using Tauc method derived from the following equation.

$$(\alpha h\nu)^{1/2} = A\,(h\nu - E_g) \qquad \textbf{(Eq. 6.2)}$$

where, α is the absorption coefficient, h is Plank's constant, ν is the frequency, A is a constant that depends on transitional probability and E_g is the optical band gap energy. The E_g was calculated by plotting hν versus $(\alpha h\nu)^{1/2}$ and extrapolating a straight line from the curve to the $(\alpha h\nu)^{1/2} = 0$ axis.

6.2.2.6.   Photocatalytic reactions

a)   Oxidation reaction of benzyl alcohol to benzaldehyde

In a typical procedure, benzyl alcohol (1 mmol, 0.108 g) was taken in a round-bottomed flask with 1 mL of acetonitrile as the solvent. Finely cut thin films of HPUNC catalyst (10 wt% with respect to benzyl alcohol were added to the flask, followed by dropwise addition of TBHP (1 mL) as the oxidant. The reaction was stirred continuously under direct sunlight and the progress of the reaction monitored by TLC. After completion of the reaction, the catalyst was isolated from the reaction by filtration. The crude reaction mixture was extracted with ethyl acetate (10 mL), washed with brine water, dried over anhydrous Na_2SO_4 and concentrated under reduced pressure. Finally the crude product was purified by column chromatography using 5-10% ethyl acetate-hexane as eluent. All the products were prepared and purified in this manner.

b)   Reduction reaction of benzaldehyde to benzyl alcohol

In a typical procedure, benzaldehyde (1 mmol, 0.106 g) was taken in a round-bottomed flask with 3 mL of isopropanol as both the solvent and the reductant. Finely cut thin films of HPUNC catalyst (7.5 wt% with respect to benzaldehyde) were added to the flask, and the vessel sealed by rubber septum. The reaction was stirred continuously under direct sunlight and the progress of the reaction was observed by TLC. After completion of the reaction, the catalyst was isolated from the reaction medium by filtration. The crude

reaction mixture was extracted with ethyl acetate (10 mL), washed with brine water, dried over anhydrous Na_2SO_4 and concentrated under reduced pressure. Finally the crude product was purified by column chromatography using 10-15% ethyl acetate-hexane as eluent. All the products were prepared and purified in this manner.

6.2.3. Characterization

FT-IR (in ATR mode), UV-Vis, XRD and TGA analysis of the oxy-g-CND and HPUNC were performed by the same instruments and under same conditions as mentioned in Chapter 2 (Section 2.2.3). TEM analysis of the oxy-g-CND and HPUNC were conducted using the same instrument and accessories, as described in Chapter 3 (Section 3.2.3). Surface area and pore volume of the HPUNC catalyst was determined by the same BET instrument and under same conditions, as mentioned in Chapter 5A (Section 5A.2.3). ^1H NMR spectroscopic characterization of the synthesized products was recorded on the same instrument, as described in Chapter 2 (Section 2.2.3) using chloroform-d_1 as the solvent. The elemental composition of the oxy-g-CND was estimated by a CHN analyzer instrument (Model: 2400 Series 2, Perkin Elmer, USA). The photoluminescence (PL) spectra of the oxy-g-CND were acquired by a fluorescence spectrophotometer (Model: Fluorolog-3, Horiba, USA). The X-ray photoelectron spectrum (XPS) of oxy-g-CND was recorded by an XPS instrument (Model: ESCALAB Xi+, Thermo Fisher Scientific Pvt. Ltd., UK). Photo-electrochemical measurements of the oxy-g-CND and HPUNC were collected on an electrochemical workstation (Model: Autolab, PGSTAT302N, Metrohm, USA), using indium tin oxide glass/glassy carbon electrode, Ag/AgCl electrode, platinum wire and aqueous Na_2SO_4 solution (0.2 M) as the working electrode, reference electrode, counter electrode and electrolyte solution, respectively. Simulated light conditions were achieved with solar simulator with a xenon arc lamp with an irradiation of 100 mW cm^{-2}. Various mechanical testing of the HPUNC films *viz.* tensile strength, elongation at break, scratch hardness, impact resistance, etc. were performed by the same instruments and under same conditions, as illustrated in Chapter 2 (Section 2.2.3).

6.3.   Results and discussion

6.3.1. Preparation and characterization of oxy-g-CND

Oxy-g-CND was prepared by microwave-assisted pyrolysis of guanidine hydrochloride and sodium citrate in an aqueous alkaline medium, as illustrated in **Scheme 6.1**. In recent times, guanidine hydrochloride has emerged as a popular choice for synthesis of graphitic carbon nitride, due to its low cost, nitrogen-rich and highly reactive nature [37].

Consequently, guanidine hydrochloride was chosen as the principal precursor. Sodium citrate played the role of surface passivating and stabilizing agent, as it contains ample carboxylic groups and hydroxyl groups that serve towards surface functionalization, as well as controlling particle size and morphology of the nanodots [38]. Further, microwave pyrolysis offers the benefit of simultaneous, homogeneous and expeditious heating, leading to uniform size distribution of the nanodots [39]. As reported in earlier work, the mechanism of formation of carbon nitride nanodots is presumed to follow a rapid pathway of cyclization and polymerization involving the precursors, to give the graphitic-carbon nitride core, made up of tri-*s*-triazine motif [1, 2].
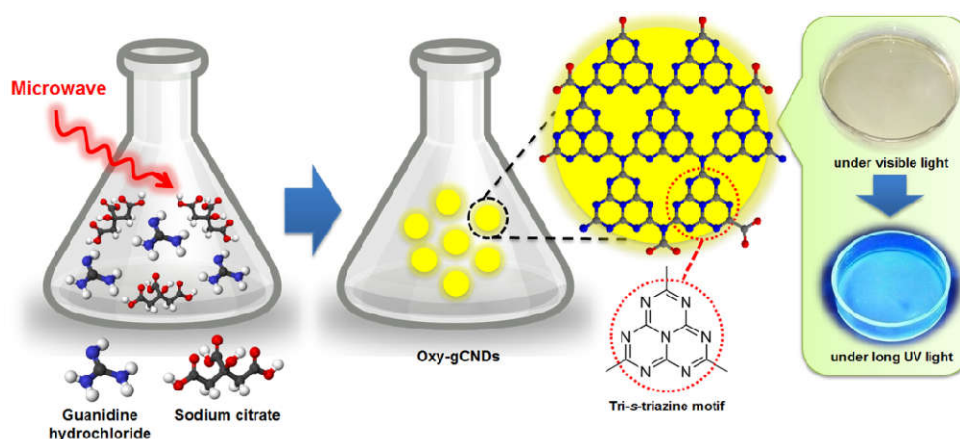
Scheme 6.1. Preparation of oxy-g-CND.

Preliminary investigations revealed that oxy-g-CND possess a yellow amorphous appearance and hygroscopic nature. These oxy-g-CNDs were found to have high dispersibility (nano-level) in water but very poor dispersibility in most of the organic solvents. The hygroscopic nature and high aqueous dispersibility indicated proper surface passivation or functionalization of graphitic carbon nitride core by oxygeneous functional groups. Remarkably, these oxy-g-CNDs exhibited high stability and good dispersibility in water even after exposure to ambient conditions for several months, without any signs of agglomeration. CHN elemental analysis of oxy-g-CND showed that the elemental weight percentages of carbon, hydrogen and nitrogen to be 24.20, 3.98 and 53.22 respectively. This indicated that oxy-g-CNDs contain rich contents of nitrogen and carbon, with a C/N ratio of 0.45. This experimental value of C/N ratio was found to be lower than theoretical value of 0.71 expected for the tri-*s*-triazine motif of graphitic carbon nitride [40]. This variation in C/N ratio clearly indicates the presence of oxygen and functionalization of oxy-g-CNDs by oxygeneous groups. ATR-FTIR spectral analysis (**Figure 6.1.a**) showed the characteristic band at 815 cm^{-1} corresponding to the tri-*s*-triazine motif of graphitic carbon nitride [37, 41], and prominent bands around 1535 cm^{-1}, 1451 cm^{-1} and 1390 cm^{-1}

attributed to typical stretching modes of CN heterocycles [41]. Additionally, occurrence of an intense sharp band at 1627 cm^{-1} corresponding to asymmetric stretching vibration of carboxylate anions and two nearby bands at 3277 cm^{-1} and 3150 cm^{-1}, corresponding to N–H stretching of primary amine group, coupled with O–H stretching of hydroxyl groups, further suggested the passivation of carboxylic and hydroxyl groups on the surface of oxy-g-CNDs. XRD pattern of oxy-g-CNDs (**Figure 6.1.b**) displayed two weak peaks centered at $2\theta = 12.6°$ and $2\theta = 23.4°$, along with a prominent sharp peak at $2\theta = 31.3°$. The peaks at 12.6° and 23.4° suggested the presence of graphitic-carbon nitride phase, corresponding to the interplanar regular stacking of conjugated CN heterocycles and interlayer stacking of aromatic layers respectively, but with considerable weaker intensities [38, 40, 41]. Further, the relatively sharp peak at 31.3° also may indicate the presence of partial graphitic sp^2 structure in the core of oxy-g-CNDs [42]. The intensities of the observed peaks were relatively low, suggesting poorly crystalline nature of the oxy-g-CNDs. Here it is pertinent to mention that some structural and ordering defects may occur during the synthetic route. The incorporation of carbon and oxygen atoms may have caused defects in the atomic arrangement, resulting in poor crystallinity [11].
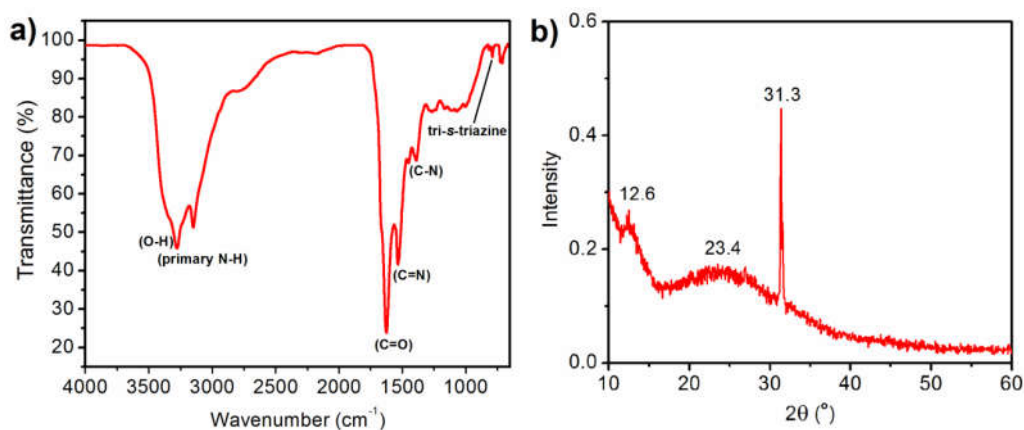

Figure 6.1. a) FT-IR spectrum, and **b)** XRD pattern of oxy-g-CND.

XPS analysis corroborated the formation of oxy-g-CNDs and provided information about their surface states. The survey spectrum (**Figure 6.2.a**) showed the four typical peaks of C1s, N1s and O1s with weight percentages of 25.7%, 37.82% and 11.53%, respectively, confirming the elemental composition of core of oxy-g-CNDs. Also, some residual impurities of Cl (196.9 eV and 269.2 eV) from guanidine hydrochloride precursor were also present on the oxy-g-CND surface. Deconvoluted high-resolution XPS spectrum of C1s (**Figure 6.2.b**) displayed several single characteristic peaks corresponding to C=C (284.6 eV), C–O (285.3 eV), C=N (288.1 eV) and C=O (288.8 eV) surface states [38, 39],

which are consistent with FTIR results. Further, the C=C peak showed higher intensity than C=O peak, confirming the presence of sp^2 graphitic structure in oxy-g-CND. Deconvoluted spectrum of O1s (**Figure 6.2.c**) further confirmed these observations with two characteristic oxygen states of C=O (531.4 eV) and C−O (532.7 eV) [40]. Deconvoluted N1s spectrum (**Figure 6.2.d**) revealed the two relative nitrogen peaks of C=N (399.8 eV) and N−H (401.5 eV) [38, 40], further confirming the presence of tri-*s*-triazine motif in oxy-g-CND. Presence of C=O, C-O and N-H bonds clearly indicated the functionalization of oxy-g-CND by carbonyl, hydroxyl and amino functional groups.
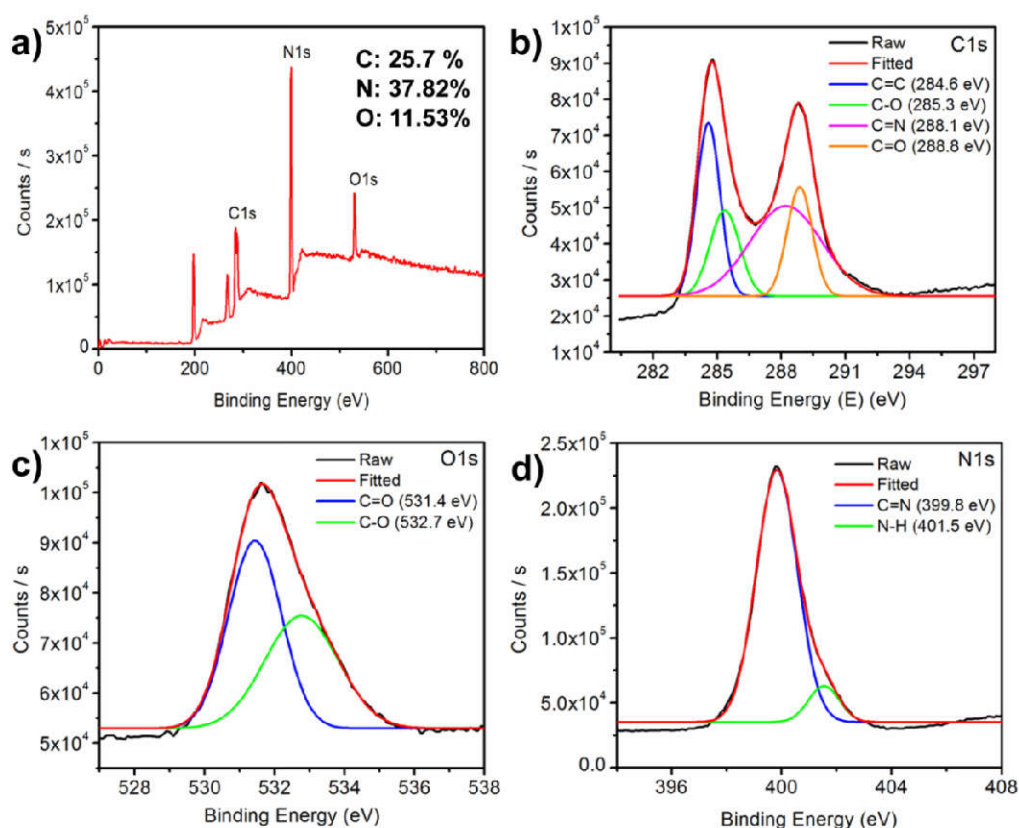
Figure 6.2. a) XPS survey spectrum of oxy-g-CND. Deconvoluted high resolution XPS spectra of **b)** C1s, **c)** O1s, and **d)** N1s of oxy-g-CND.

Similar to most of the carbon quantum nanodots, these highly water dispersible oxy-g-CNDs show remarkable optical properties. These nanodots displayed high nano-level aqueous dispersion and multi-colored emissions, appearing yellow under visible light, green under short UV light (254 nm) and bright cyan under long UV light (365 nm) (**Figure 6.3.a**). UV-Visible spectral analysis of oxy-g-CNDs (**Figure 6.3.b**, **red line**) showed the characteristic bands of graphitic-carbon nitride – a strong band centered at 235 nm corresponding to $\pi \rightarrow \pi^*$ transition of tri-*s*-triazine motif, followed by a continuous weak

band from 290 nm that extended upto 490 nm in visible region, corresponding to $n \rightarrow \pi^*$ transitions originating from surface passivating functional groups of oxy-g-CNDs [37]. PL study of oxy-g-CNDs (**Figure 6.3.b, blue line**) showed a narrow and symmetrical maximum PL emission band centered at 445 nm upon excitation at 360 nm, which can be held responsible for the bright cyan PL emission. Notably, the quantum yield of oxy-g-CNDs (λ_{ex} =360 nm) was measured to be 19%, using quinine sulfate as a standard [37]. Furthermore, oxy-g-CNDs revealed notable variations in PL emission upon varying the excitation wavelength from 300 nm to 500 nm (**Figure 6.3.c**), as the PL emission peak was red-shifted from 435 nm to 540 nm, while its intensity increased and then decreased gradually. These results suggested that oxy-g-CNDs exhibited excitation wavelength-dependent PL behavior, owing to the effects of optical selection of differently-sized nanoparticles (quantum confinement effect) and considerable distribution of surface states and emissive traps sites on the oxy-g-CNDs surface, similar to most of carbon quantum dots [43, 44]. Moreover, these oxy-g-CNDs displayed good photostability (**Figure 6.3.d**), as the PL intensity remained constant upto 2 h under exposure of continuous 365 nm excitations.
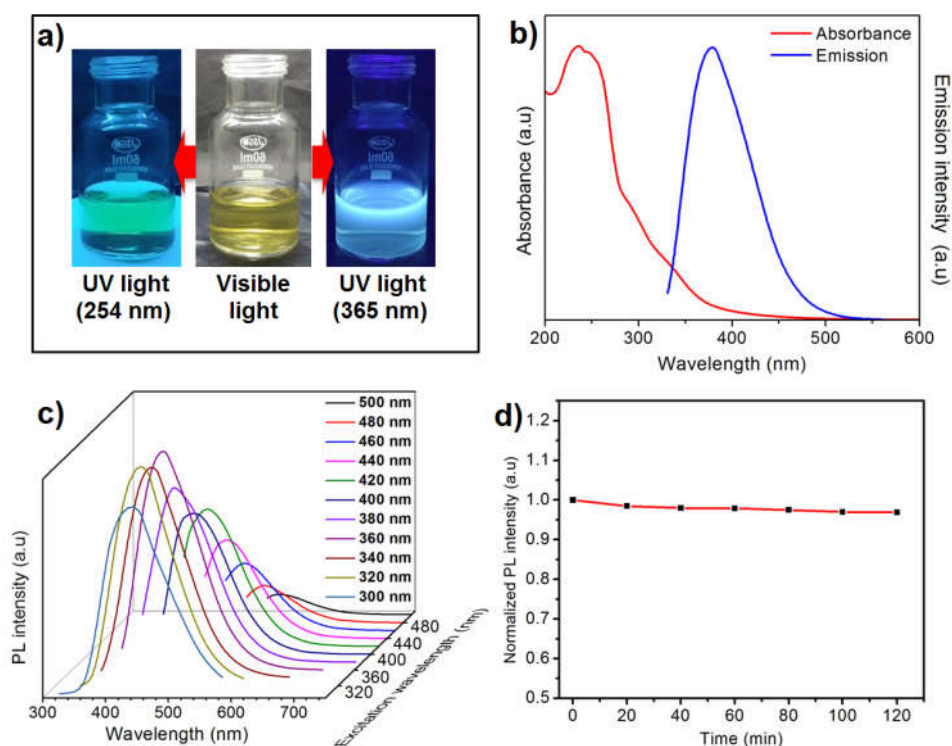

Figure 6.3. a) Aqueous dispersion of oxy-g-CNDs under UV light and visible light, **b)** UV-Vis absorbance (red line) and PL emission (blue line, λ_{ex}=360 nm) spectra of oxy-g-CNDs, **c)** PL emission spectra of oxy-g-CNDs at different excitation wavelengths, and **d)** Change in PL emission intensity upon exposure to continuous excitation at wavelength of 360 nm for 2 h.

TEM analysis showed that the as-prepared oxy-g-CNDs were mono-dispersed with very little signs of aggregation (**Figure 6.4.a**). HRTEM image of an individual oxy-g-CND showed spherical morphology and presence of well-defined lattice fringes (**Figure 6.4.b**). Corresponding IFFT image of the oxy-g-CND phase revealed clear lattice fringes with an inter-planar spacing of 0.24 nm (Figure 6.4.b, inset), consistent with the (1120) facet of graphene [43, 44]. This indicated the presence of graphitic sp^2 carbon atoms in the core of the oxy-g-CND, as earlier indicated by XRD analysis. SAED pattern further showed weak diffraction rings, indicating poorly crystalline nature of the oxy-g-CNDs (**Figure 6.4.c**), as previously indicated by XRD analysis. Statistical analysis further showed the size distribution of oxy-g-CNDs within the narrow range of 1-3 nm, with average size of *ca.* 2.2 nm (**Figure 6.3.d**).
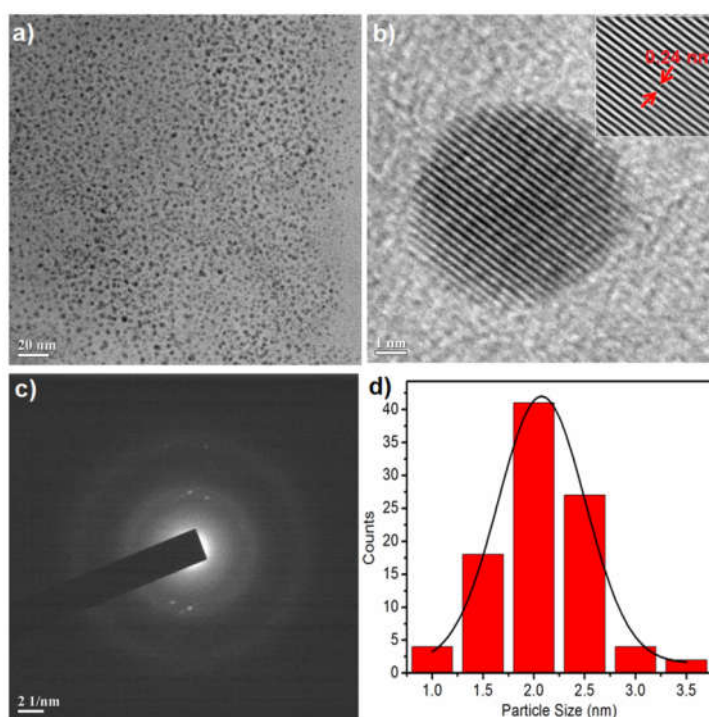
Figure 6.4. a) TEM image of oxy-g-CNDs at magnification of 20 nm, **b**) HRTEM image of oxy-g-CND at magnification of 1 nm (inset: IFFT image of oxy-g-CND phase), **c)** SAED pattern of oxy-g-CND, and **d)** Particle size distribution of oxy-g-CND.

6.3.2. Fabrication and characterization of HPU/oxy-g-CND nanocomposite

HPU/oxy-g-CND nanocomposite was fabricated by an *in situ* polymerization technique using varying loadings of oxy-g-CNDs as the nano-reinforcing agent, as shown in **Scheme 6.2**. Formation of HPUNC depends on several factors, most importantly the concentration of reactants and dispersion of the nanomaterial in the polymer matrix [44, 45]. The

concentration of the reactants, especially branching moiety was maintained by dilution with solvent during polymerization reaction. This strategy allowed the smooth completion of the reaction without any gel formation, which is a usually encountered problem during formation of hyperbranched polymer. Further, uniform dispersion of the nanomaterial in the polymer matrix is an important condition for formation of polymeric nanocomposite [45]. The nano-reinforcing agent was properly dispersed in solvent by ultrasonication, prior to its addition in the polymerization reaction. Oxy-g-CNDs, by the virtue of its surface passivating functional groups, formed a stable dispersion in DMF for a short time, allowing timely addition in the reaction. Moreover, the nano-reinforcing agent was judiciously added to the pre-polymer in the beginning of the second step with vigorous mechanical shearing force. This tactic aided in the assimilation of the nanodots in the pre-polymer and resulted in the formation of a uniformly dispersed nanocomposite.
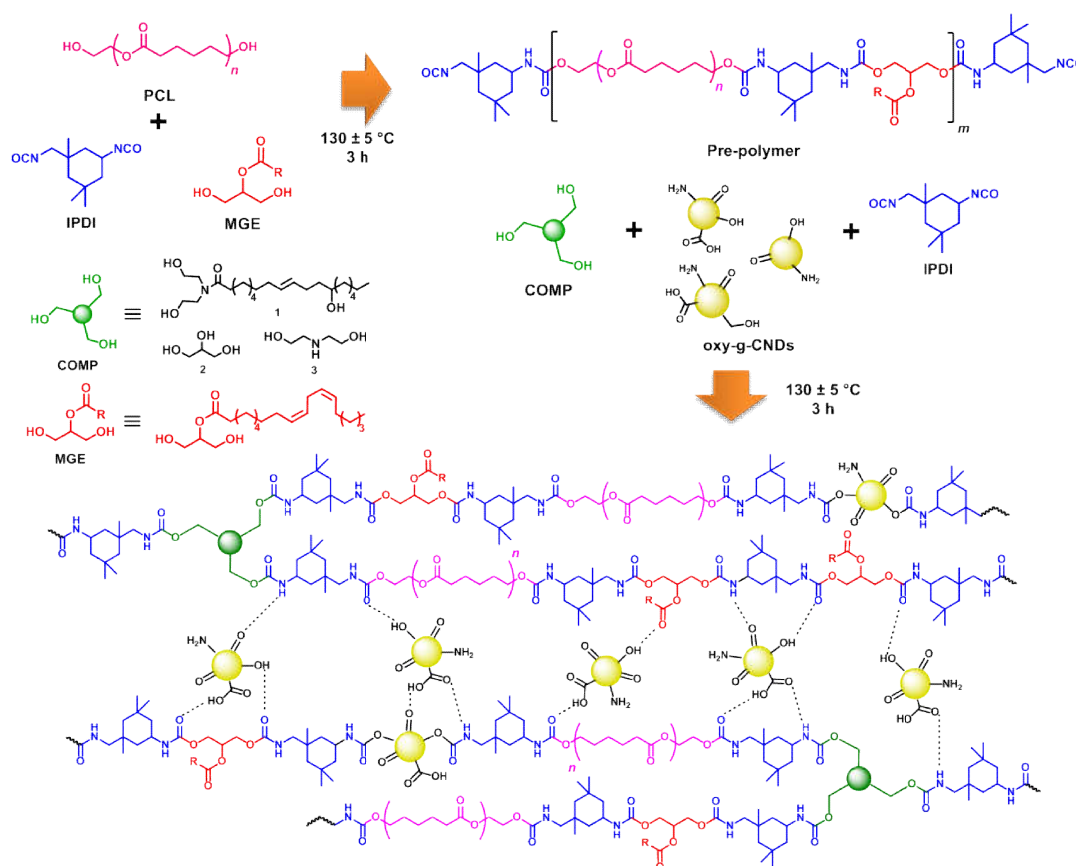
Scheme 6.2. Fabrication of HPU/oxy-g-CND nanocomposite.

ATR-FTIR spectra of the initial pre-polymer, HPU and HPUNCs revealed key changes in chemical functionalities which suggested the formation of the polyurethane linkages, as illustrated in **Figure 6.5.a**. The FTIR of the pre-polymer revealed the

appearance of bands of –NH stretching at 3421 cm^{-1} and free -C=O band at 1736 cm^{-1} prominently, along with free isocyanate (-NCO) band at 2260 cm^{-1} indicating the formation of the isocyanate-terminated polyurethane pre-polymer as depicted in first step of the fabrication process in Scheme 6.2. The bands of polyurethane further became more conclusive and prominent in the FTIR of the HPU and HPUNC after the second step of the fabrication process. The broad band centered at 3362 cm^{-1} was attributed to N-H stretching vibration of the urethane linkage, coupled with O-H stretching vibration. The sharp band at 1724 cm^{-1} juxtaposed with the weak band at 1640 cm^{-1} was alluded to free C=O and H-bonded C=O stretching vibration of urethane linkage respectively. Further, the medium intensity band at 1530 cm^{-1} was attributed to the coupled vibrations of N-H bending and C-N stretching of the urethane linkage, while the medium intensity band at 1240 cm^{-1} was ascribed to the C-O-C stretching vibrations of urethane linkage, correspondingly. At the same time, the medium intensity band at 1045 cm^{-1} was ascribed to C-O stretching vibration of the urethane linkage. Additional bands were observed prominently at 2938 cm^{-1} and 2865 cm^{-1} corresponding to the asymmetric and symmetric C-H stretching vibrations of –CH$_2$ and –CH$_3$ groups of the polyurethane chain segments. Other C-H modes of vibrations, resulting from the chain segments of HPUNC were also observed distinctly in the spectra at 1465 cm^{-1} (–CH$_2$ scissoring coupled with –CH$_3$ asymmetric deformation), 1366 cm^{-1} (–CH$_3$ symmetric deformation), 1295 cm^{-1} (–CH$_2$ wagging) and 730 cm^{-1} (–CH$_2$ rocking in long aliphatic chains). Most notably, the band observed for free –NCO group at 2260 cm^{-1} disappeared completely, suggesting complete and quantitative formation of HPUNC. X-ray diffractograms of HPUNC, as shown in **Figure 6.5.b**, clearly indicated the presence of crystallinity. Two strong diffractions peaks were observed at $2\theta = 21.5°$ (calculated *d*-spacing of 4.12 Å) and $2\theta = 23.8°$ (calculated *d*-spacing of 3.73 Å), due to (110) and (200) planes of crystalline PCL moiety, respectively [44, 45]. In addition, enhancement in peak intensity of PCL moiety with incorporation of the nano-reinforcing agent was observed. This enhancement can be attributed to the good nano-reinforcing effect of the oxy-g-CND. This nano-reinforcing ability was reflective of the strong physico-chemical interactions between the near-graphitic nanomaterial and the crystalline segments of the polymer chains. Further, the nanocomposites displayed slight enhancement of peak intensity upon increasing the loading capacity of the nano-reinforcing agent. Calculation of % crystallinity of the nanocomposites using peak integration function in Origin® 8.5 affirmed this observation with corresponding values of 22.1% (0.5 wt%), 22.6% (1.0 wt%) and 23.5% (2.0 wt%), compared to that of 21.95% of only pure HPU. Hence, it can be stated that, as the loading of oxy-g-CND increased in the polymer matrix, the extent of these physico-chemical interactions also increased, imparting better

reinforcement of HPU matrix. TEM images of HPUNC1.0 in **Figure 6.5.c** revealed the consistent dispersion of oxy-g-CND (red circles) in the HPU matrix, conclusively indicating the formation of the nanocomposite.
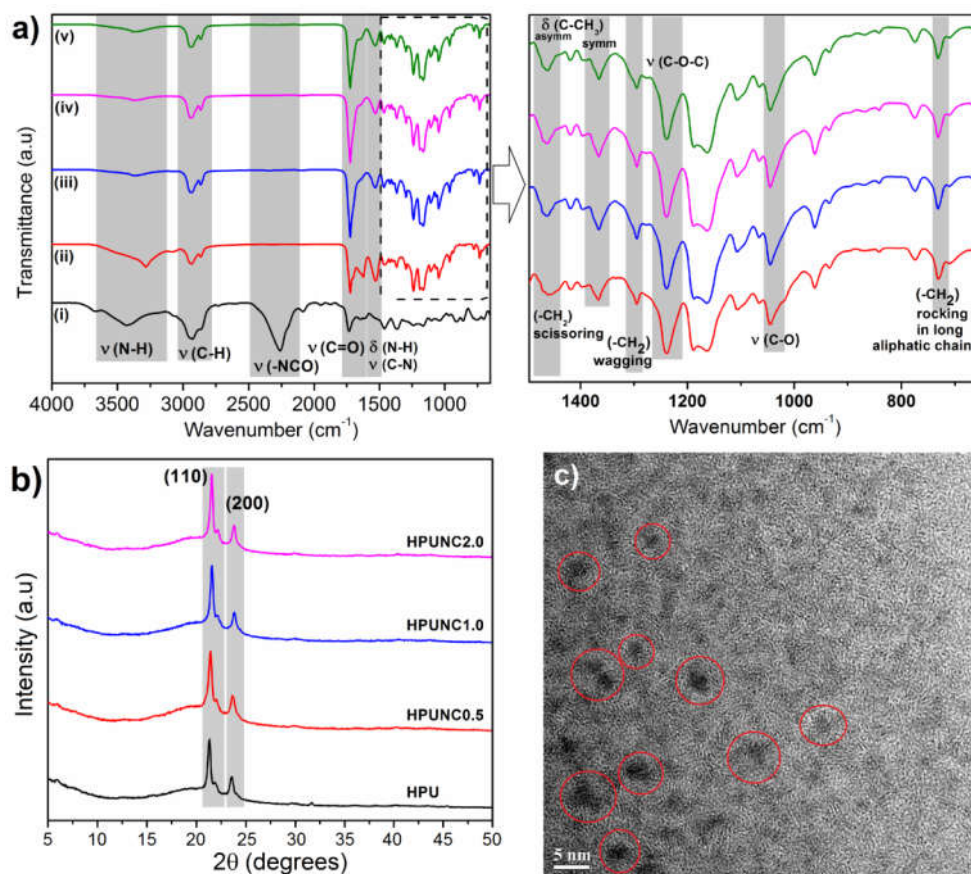

Figure 6.5. a) ATR-FTIR spectra of (i) Pre-polymer, (ii) HPU, (iii) HPUNC0.5, (iv) HPUNC1.0 and (v) HPUNC2.0 with magnification of 1500 cm^{-1}-500 cm^{-1} region, **b)** XRD patterns of HPU and HPUNCs, and **c)** HR-TEM image of HPUNC1.0 at magnification of 5 nm.

6.3.3. Mechanical properties

The mechanical properties of HPUNC were evaluated and demonstrated in **Table 6.1**. Mechanical properties like tensile strength, elongation at break, toughness, scratch hardness and impact strength were significantly improved, even at very low nanomaterial loading. Further, the nanocomposites displayed loading-dependent improvement of mechanical properties. The stress-strain profiles of HPU and its nanocomposites shown in **Figure 6.6.a**, as well as effect of nanomaterial loading on tensile strength (**Figure 6.6.b**), elongation at break (**Figure 6.6.c**) and toughness (**Figure 6.6.d**), highlighted the reinforcing effect of oxy-g-CNDs.

The tensile strength of the nanocomposite improved gradually on increasing the nano-reinforcing agent loading from 0.5 wt% to 2.0 wt%, showing maximum enhancement upto 1.9 fold. At the same time, elongation-at-break of the nanocomposite also improved slightly on gradual increase of nano-reinforcing agent loading, displaying maximum enhancement upto 1.2 fold. The values of toughness, calculated by integration of the area under curve from the stress-strain profile of HPUNCs, also showed improvement upto 2.5 fold with increasing nano-reinforcing agent loading. Further, the nanocomposite displayed improved values of scratch hardness and impact resistance, which could not be precisely quantified as they exceeded the maximum limit of the instruments. This improvement in the mechanical properties of the nanocomposites can be solely attributed to the presence of the oxy-g-CNDs in the HPU matrix, and strong interfacial interactions existing between them. At this juncture, it is pertinent to know that carbon nanostructures can act as very good reinforcing material for polymers, due to their structural stability and compatibility [46]. In this context, oxy-g-CNDs served the role of suitable nano-reinforcing agent, as they possess a formidable semi-carbonized structural motif as well as various surface passivating functional groups which provided rigidity and flexibility to the polymer matrix by participating in various physico-chemical interactions within the polymer matrix. This oxy-g-CNDs reinforced-HPU matrix, hence contributed to its high performance.

Table 6.1. Mechanical properties of HPU and its nanocomposites

Parameter	HPU	HPUNC0.5	HPUNC1.0	HPUNC2.0
Tensile strength (MPa)	5.3±0.2	6.4±0.1	8.5±0.2	12.0±0.1
Elongation at break (%)	610±5	637±10	676 ±5	732±2
Toughness^a (MJm^{-3})	28.34	35.56	58.24	72.20
Scratch hardness^b (kg)	10	>10	>10	>10
Impact strength^c (kJm^{-1})	19.02	20.92	20.92	20.92

^{a}Calculated by intergrating the stress-strain profiles of HPUNCs. ^{b}maximum limit of the instrument is 10 kg. ^{c}calculated by converting into energy unit as per thickness between 0.43-0.45 mm.

Recent state of art literature endorses the reinforcing role of such carbon quantum nanodots-like materials with various polymeric materials. For example, Gobi and co workers showed that incorporation of 2.5 wt% of graphene quantum dots in an epoxy resin led to a 2.25 fold increase in tensile strength, 1.18 fold increase in nominal strain-at-break and 2.6 fold increase in toughness [47]. In another instance, Zhang et al. reported that

inclusion of 2 wt% carbon quantum dots in an epoxy resin resulted in 1.39 fold increment in tensile modulus [48]. Seminal works done by the author's group towards development of high performance hyperbranched polymer nanocomposites with carbon quantum dot nanomaterials are also noteworthy. For instances, a hyperbranched epoxy resin nanocomposite with 1 wt% carbon dots showed improvement of 1.22 fold in tensile strength, 1.21 fold in elongation-at-break and 1.17 fold in toughness [49]; a hyperbranched waterborne polyurethane nanocomposite containing 1 wt% of carbon dots displayed enhancements of 1.8 fold in tensile strength and 1.41 fold in elongation-at-break [44]; a hyperbranched waterborne polyester nanocomposite containing 1 wt% carbon dots demonstrated very high enhancements of 6.02 fold in tensile strength and 2.8 fold in toughness [50]. In overall, these reports reiterated the role of carbon quantum nanodots as capable reinforcing agents for polymers and substantiated the results were observed for HPUNCs.
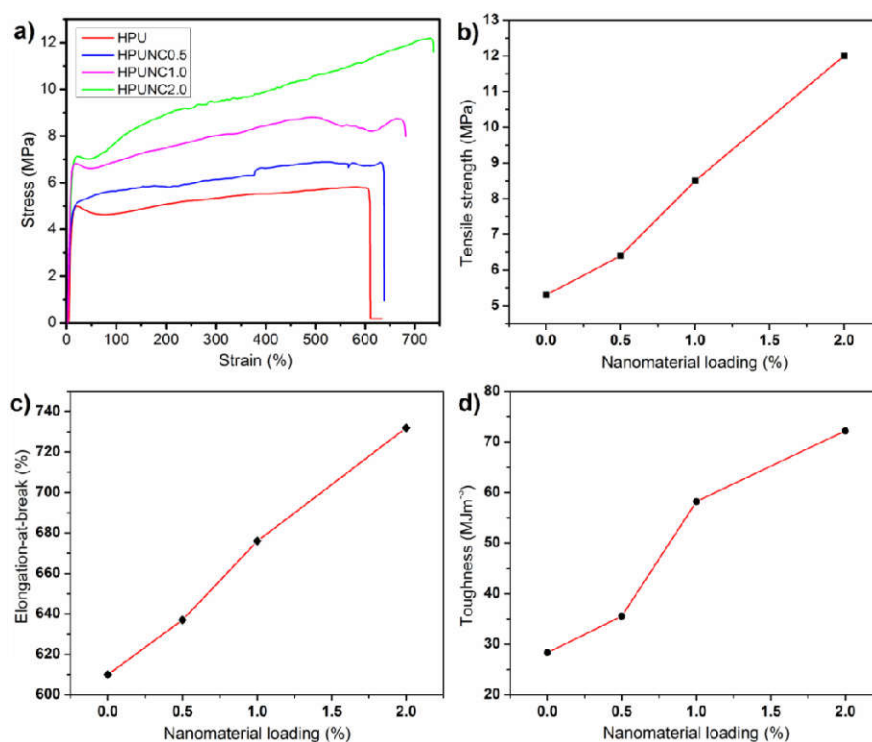
Figure 6.6. a) Stress-strain profiles of HPU and HPUNCs, and effect of nanomaterial loading on, **b)** tensile strength, **c)** elongation-at-break, and **d)** toughness.

6.3.4. Thermal properties

The thermal properties of HPUNCs were evaluated by thermogravimetric analysis. The TG curves of HPUNCs along with HPU and oxy-g-CNDs are shown in **Figure 6.7**. The

nanocomposites displayed slight and gradual improvement in thermal degradation temperature at a very low loading of nano-reinforcing agent. In addition, all the nanocomposites displayed enhancement of degradation temperatures corresponding to the loading of the nano-reinforcing agent. This enhancement in thermal degradation temperatures can be mainly attributed to the presence of oxy-g-CNDs nano-reinforcing agent in the HPU matrix and their reinforcing effect on the matrix. Here, it is pertinent to mention that graphitic carbon nitride possess a host of unique properties including excellent thermal stability, owing to it near-graphitic core structure [6, 7]. Therefore, the dispersion of oxy-g-CNDs in the polymer matrix imparted a stabilizing effect on the polymer matrix by absorbing the thermal energy in its core. In addition, reinforcement of the HPU matrix by oxy-g-CNDs led to occupation of free volume available in the matrix, thereby restricting the arbitrary motion of the polymeric chains under thermal energy. This reinforcement ultimately imparted resistance to the degradation of the polymer matrix.
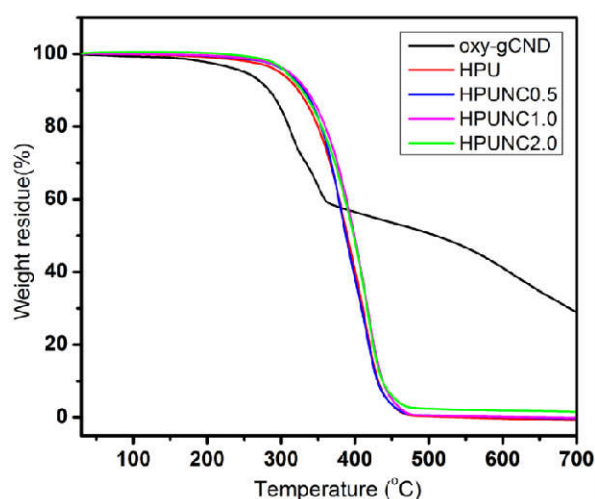
Figure 6.7. TG curves of oxy-g-CND, HPU and HPUNCs.

6.3.5. Anti-counterfeiting application

HPU/oxy-g-CND nanocomposite was dispersible in polar aprotic solvents like THF, DMF, DMSO, etc. displaying a light yellow transparent solution. This solution transparency can be combinely attributed to the aliphatic nature of the HPU matrix and quantum size effect of the oxy-g-CNDs. In addition, the dispersed nanocomposite was found to exhibit bright cyan photoluminescence, owing to the presence of oxy-g-CNDs in the polymer matrix. The transparency and photoluminescent property of HPUNC make the corresponding dispersion as a suitable material for anti-counterfeiting tool, as such the material is hard to replicate and process. As shown in **Figure 6.8.a**, the HPUNC dispersion in xylene is light

yellow in color in daylight but emits bright cyan emission under long UV light (365 nm). This HPUNC dispersion can be filled into a gel/sketch pen refill and utilized directly as ink. To demonstrate the performance of nanocomposite as an anti-counterfeiting ink, the characters "TU" and "APNL" were written on commercially available filter paper and the characters "HPUNC" written on a sheet of ordinary plastic using a sketch pen filled with the nanocomposite ink. The characters were not observed by the naked eye in the normal daylight; but were clearly visible in PL mode (bright cyan color) under illumination of a 365 nm UV lamp, as visualized in **Figure 6.8.a** (top and bottom). Most importantly, this ink was stable for several months in ambient conditions and applicable on different surfaces like paper and plastic. Moreover, the nanocomposite ink also exhibited reinforcing effect on the coated material. This reinforcing effect was confirmed by evaluating the mechanical property of commercial filter paper coated with the ink. As evident from the stress-strain profile in **Figure 6.8.b**, the tensile strength of HPUNC ink coated paper manifolded by 2.14 times, while the elongation at break drastically improved by 3.82 times, signifying excellent reinforcing ability of the ink. The improved physico-mechanical property of the nanocomposite ensured stability of the nanocomposite and protection of the coated material and its content towards any external forces or any kind of wear or tear, to some extent. Moreover, bio-derived nature of the nanocomposite, its intricate design and processing endowed eco-friendliness and exclusivity, respectively. These observations reiterated the potential utility of HPUNC dispersion as a high performance anti-counterfeiting ink that can be used for loading important information for secret communications and security features.
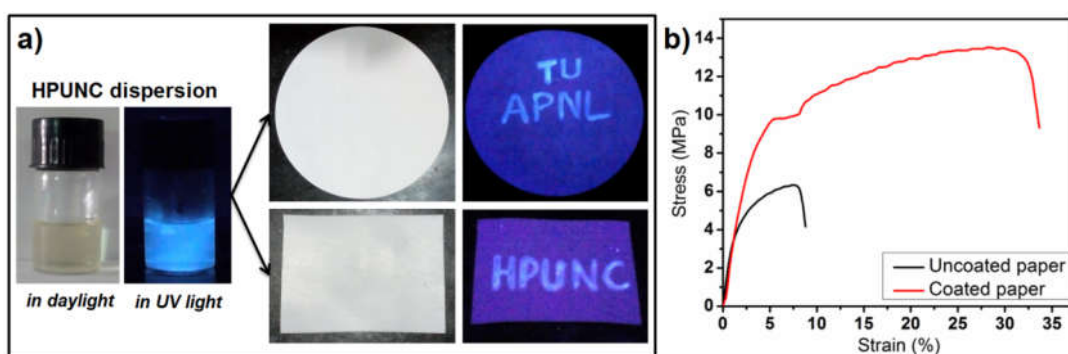

Figure 6.8. a) Photographs of dispersion of HPUNC in xylene under daylight and long UV light (365 nm), (at top) handwritten characters with HPUNC ink on commercially available filter paper under daylight and long UV light (365 nm), (at bottom) handwritten characters with HPUNC ink on ordinary plastic sheet under daylight and long UV light (365 nm), and **b)** Stress-strain profile of HPUNC ink coated paper and uncoated paper.

6.3.6. Photocatalytic application

Before proceeding to investigate the photocatalytic activity of the HPUNC nanocomposite, we evaluated certain parameters that ensured its suitability as a heterogeneous photocatalytic system. By convention, the activity of a photocatalyst is mainly dependent upon its light absorption and light harvesting abilities [16]. The overall photoactivity involves three processes: generation, separation and recombination of charge carriers or electron-hole pairs. Absorption of light (photons) generates charge carriers by photo-excitations, which would rapidly undergo radiative (PL) or non-radiative recombination [16]. The efficiency of a photocatalyst is improved by rapid separation of charge carriers and their delayed recombination. By the virtue of their molecular framework and quantum dimension, g-CN possesses the ability to absorb and harvest light over the solar spectrum (covering most of the UV-Vis spectral region) in conformity with their photo-excited states [3, 4]. Recent studies indicate the role of photo-generated charge carriers by photo-excitation of g-CN surface in their photoactivity [3-5]. The radiative recombination of these charge carriers, trapped at different surface sites is reflected in their PL emission [5, 18]. In this context, the light absorption ability and the role of photo-generated charge carriers in oxy-g-CNDs were investigated by optical and electrochemical studies. The absorption of suitable radiation is vital for any photocatalyst. UV-Visible absorbance spectrum of HPUNC (**Figure 6.9.a**) suggested its superior ability to absorb radiation in the UV and visible light range than bare oxy-g-CNDs, which augured well for photo-catalytic activity. The broad absorbance of HPUNC can be possibly attributed to electronic transitions of the HPU matrix, whose intensity overwhelms the transitions of oxy-g-CNDs. HPU matrix contains surface functional moieties like $-NH-C(=O)-O-$, $-O-C=O$, $-OH$, $-NH$, etc. [35, 36], which can lead to suitable light absorption. The possession of a favorable optical band gap is a crucial criterion for any photocatalyst. Generally, the entire spectrum of solar light, from infrared to ultraviolet, covers a range of about 0.5 eV to about 2.9 eV [17]. Any photocatalyst with a band gap within this range possess the ability to absorb and harvest solar light. Band gap calculation of oxy-g-CND and HPUNC using Tauc method (**Figure 6.9.b**) revealed almost comparable optical band gaps of 2.93 eV and 2.57 eV, which are well within the permissible range. This suggested that the light absorbing ability of the oxy-g-CND remained intact even after formation of the nanocomposite. The corresponding VB and CB potentials of oxy-g-CND were estimated to be 1.325 eV and −1.605 eV, calculated in accordance to a previous report [20]. As already discussed earlier in the chapter, PL studies suggested the role of photo-induced charge carriers in oxy-g-CND and supported its suitability for photocatalytic activity. Electrochemical impedance spectroscopy (EIS) further corroborated the photo-

activity of oxy-g-CNDs from their charge transfer behaviour in electrolyte solution, under simulated light and dark conditions. EIS plots of oxy-g-CND (**Figure 6.9.c**) displayed an obvious smaller arc radius under simulated light conditions compared to dark conditions. Since the diameter of the arc reflects the resistance of charge transfer between electrode surface and electrolyte solution [21]. The relatively smaller arc radius of oxy-g-CND under simulated light conditions suggested improved charge transfer of photo-generated charge carriers at surface/interface. Chronoamperometric curves of oxy-g-CND (**Figure 6.9.d**) suggested the ample contribution of photocurrent to the total current density. The corresponding curves with intermittent illumination for 10 s in repeated on-off cycles demonstrated rapid and consistent transitory photocurrent responses, indicating good efficiency for the separation of photo-generated charge carriers and their transfer. Ultimately, the optical and electrochemical studies of oxy-g-CNDs put forth a compelling evidence of its photo-harvesting nature.
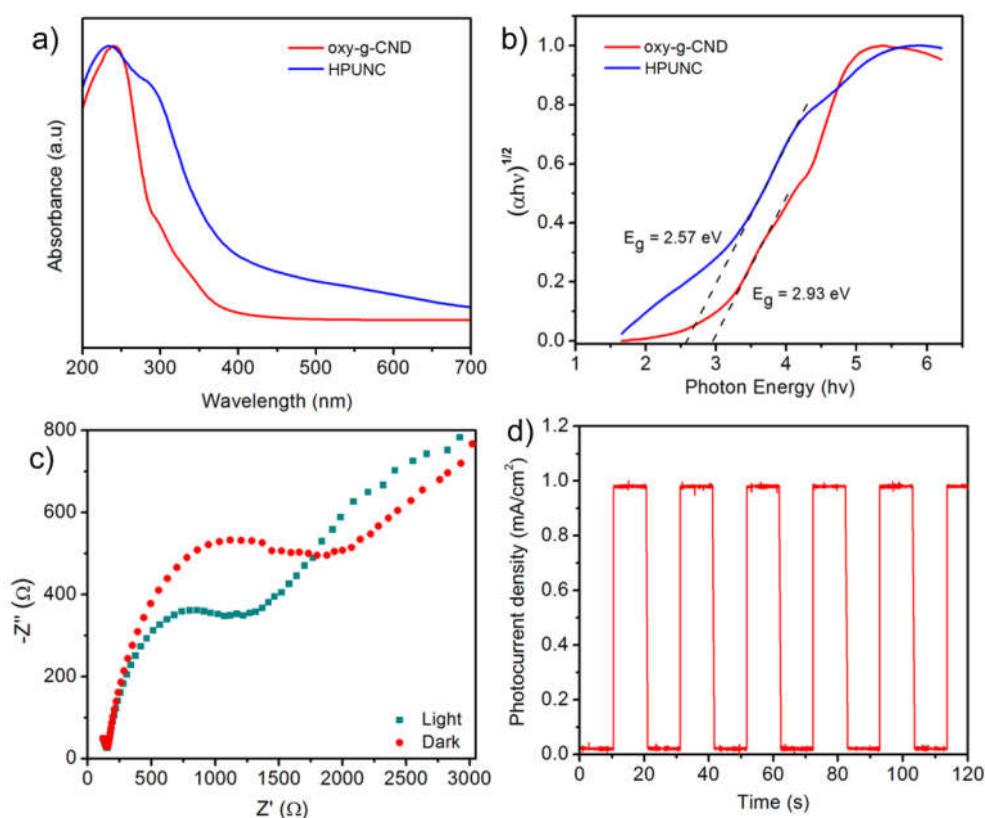
Figure 6.9. a) UV-Vis spectra of oxy-g-CND and HPUNC, **b)** Tauc plots of oxy-g-CND and HPUNC, **c)** EIS plots of oxy-g-CND under simulated light and dark conditions in the frequency range from 10 mHz to 10 μHz with a 50 mV sinusoidal AC voltage, and **d)** Chronoamperometric curves of oxy-g-CND at a fixed potential of 0.5 V with intermittent irradiation cycles.

We initially opted to investigate the feasibility of HPUNC as photocatalyst in oxidation of benzyl alcohol to benzaldehyde as the model reaction, using direct sunlight as the energy source. Surprisingly, the reaction delivered benzaldehyde exclusively as the product, in the presence of H_2O_2 as oxidant and H_2O as the solvent. Encouraged by this result, we set to optimize the reaction conditions by varying the parameters like solvent, oxidant and catalyst loading and the results are summarized in **Table 6.2**.

Table 6.2. Optimization of reaction conditions[a] for oxidation of benzylic alcohol

Entry	Catalyst (wt%)	Oxidant	Solvent	Time (h)	Yield[b] (%)
1	5.0	H_2O_2	H_2O	12	15
2	5.0	H_2O_2	EtOH	12	20
3	5.0	H_2O_2	PhMe	12	Trace
4	5.0	H_2O_2	$CHCl_3$	12	Trace
5	5.0	H_2O_2	THF	8	25
6	5.0	H_2O_2	MeCN	6	40
7	5.0	H_2O_2	DMF	8	35
8	5.0	NaOCl	MeCN	5	50
9	5.0	TBHP	MeCN	3	50
10	7.5	TBHP	MeCN	3	70
11	10.0	TBHP	MeCN	3	90
12	12.0	TBHP	MeCN	3	90
13	-	TBHP	MeCN	12	Trace
14	10.0	-	MeCN	12	NR#
15[c]	10.0	TBHP	MeCN	12	Trace
16[d]	10.0	TBHP	MeCN	12	Trace
17[e]	10.0	TBHP	MeCN	12	70[f]
18[g]	10.0	TBHP	MeCN	3	30

[a]Reaction conditions: Benzyl alcohol (1 mmol, 0.108 g), HPUNC catalyst (in wt% with respect to substrate), oxidant (1 mL, 30%v/v H_2O_2/ 4%w/v NaOCl/ 70%v/v TBHP), solvent (1 mL). [b]Isolated product, confirmed by TLC using authentic substrate. [c]Under dark condition. [d]HPU used as catalyst. [e]oxy-g-CND (in 1 mL H_2O) used as catalyst. [f] Mixture of products. [g]In presence of TEMPO. #No reaction.

Different solvents were screened for the model reaction. The reaction was found to proceed sluggishly in protic solvents like H_2O and EtOH (Table 6.2, Entry 1, 2). Use of less polar solvent like toluene and halogenated solvent like $CHCl_3$ was found to be grossly insufficient for the model reaction (Table 6.2, Entry 3 & 4). The model reaction afforded better results with aprotic solvents like THF, MeCN and DMF (Table 6.2, Entry 5-7), with MeCN providing a modest 40% yield. We further performed the model reaction with different oxidants. The oxidant plays a crucial role in ensuring the selectivity and productivity of reaction. Use of H_2O_2 as the oxidant was less effective, as the model reaction could not deliver more than a modest yield of 40% (Table 6.2, Entry 6). The reaction fared better with NaOCl as the oxidant, producing 50% yield (Table 6.2, Entry 8). However, the reaction performed extremely well in the presence of TBHP as oxidant, generating a comparable 50% yield in much shorter time (Table 6.2, Entry 9). Hence, the order of activity of oxidant can be summarized as, TBHP<NaOCl<H_2O_2. A more rational explanation of this order can be provided by the relative stability of the oxidizing species. TBHP forms a comparatively more stable but sterically hindered radical species [51], than the corresponding homologues of NaOCl and H_2O_2. Also, another reason for low effectiveness of H_2O_2 can be attributed to the rapid photodecomposition of the oxidant under direct sunlight. H_2O_2 readily undergoes decomposition to O_2 and H_2O under direct photoconditions, thereby being unable to complete the reaction [52]. Next, we set to investigate the influence of catalyst loading on the model reaction. Catalyst loading of 5 wt% delivered the selective product with 50% yield (Table 6.2, Entry 9). On increasing the catalyst loading to 7.5 wt%, the efficiency of the reaction improved producing 70% yield (Table 6.2, Entry 10). Catalyst loading of 10 wt% was found to be optimum amount for the photo-catalyzed oxidation with 90% yield (Table 6.2, Entry 11), as further increase in catalyst loading to 12 wt% didn't improve the efficiency of the reaction (Table 6.2, Entry 12). As expected, the model reaction failed to deliver under neat conditions without any catalyst or oxidant (Table 6.2, Entry 13, 14), signifying the vital importance of the catalyst and oxidant to complete the reaction. Additionally, the model reaction was also tried under dark conditions, yielding trace amount of product (Table 6.2, Entry 15). This reiterated the role of the sunlight as a crucial parameter for driving the photo-catalyzed reaction. Sunlight is preferred over other photo-sources like UV, as it is universal, renewable and green energy source. On using bare HPU as the catalyst, the model reaction gave traces of product (Table 6.2, Entry 16). This exemplified the role of the photo-active component oxy-g-CND for energizing the reaction, and HPU solely cannot be accountable for the productivity. Further, the model reaction was investigated using bare oxy-g-CND as the photocatalyst. Interestingly, the reaction with 10 wt% oxy-g-CNDs afforded a mixture of products, with an

overall isolated yield of 70% (Table 6.2, Entry 17). However, the separation and recovery of the highly water dispersible oxy-g-CND catalyst became an arduous task after the completion of the reaction. This observation signified that the exclusive selectivity and heterogeneity of the model reaction depended upon HPU component, rather than oxy-g-CND. The tandem participation of both the components is vital for the selectivity and efficiency of the oxidation reaction. When the model reaction was enacted in the presence of a free radical scavenger, (2,2,6,6-Tetramethylpiperidin-1-yl)oxyl (TEMPO), the reaction was severely quenched, furnishing no more than 30% of the selective product (Table 6.2, Entry 18). This indicated the role of free radical oxidizing species generated in the reaction medium being responsible for the formation of the oxidized product.

Upon the recognition of the optimized conditions, we proceeded to explore the generality of the HPUNC-photocatalyzed selective oxidation of differently substituted benzyl alcohols and the results are reflected in **Table 6.3**.

Table 6.3. Substrate study for oxidation of benzylic alcohols

Entry	Reactant	Product	Yield[b] (%)
1a			90
1b			95
1c			92
1d			75
1e			78
1f			NR#
1g			NR#

[a]Reaction conditions: Benzylic alcohol derivative (1 mmol), TBHP (1 mL, 70%v/v), MeCN (1 mL), HPUNC catalyst (10 wt%), under sunlight, 3 h. [b]Isolated product, purified by column chromatography and identified by ^{1}H-NMR analyses (Page 6-36–6-38). #No reaction.

As demonstrated in Table 6.3, HPUNC was established as a robust, sustainable and efficient photocatalyst for the selective oxidation of benzyl alcohol derivatives, delivering the oxidized product in good to high yields, in most of the cases (Table 6.3, Entry 1a-1e). The electronically diverse substituents attached to the benzylic alcohols exhibited their influence on the overall efficiency of the protocol, with the reaction being productive in case of substrates with electron releasing substituents than electron withdrawing ones. However, it is worthwhile to mention that the optimized conditions failed to evoke any productivity in case of aliphatic hexan-1-ol (Table 6.3, Entry 1f) and heteryl indol-3-carbinol (Table 6.3, Entry 1g). Nevertheless, the scope of metal-free heterogeneous HPUNC photocatalyst was successfully applicable to benzyl alcohols derivatives with high selectivity and productivity.

Thereafter, we also opted to probe the utility of the HPUNC as photocatalyst in the reverse reaction under direct sunlight. We, at first tried to optimize the reaction conditions by considering the reduction of benzaldehyde to benzyl alcohol as the model reaction using alcoholic solvents and HPUNC as the catalyst under direct sunlight. The results are summarized in **Table 6.4**. Solvent screening of the reaction showed that the reaction yielded high productivity in alcoholic solvents like MeOH, EtOH and *i*PrOH than any other solvents (Table 6.4, Entry 1-9) with optimum productivity achieved in *i*PrOH. Alcoholic solvents act as good electron donors and hydrogen sources [37-40]. The reaction did not proceed in H_2O possibly due to its poor proton donor ability and poor miscibility of the organic substrate. Less polar and halogenated solvents like toluene and $CHCl_3$ respectively were also unable to deliver the reaction (Table 6.4, Entry 5-6), probably due to poor hydrogen releasing abilities. Due to similar reasons, the model reaction also did not progress favorably in aprotic solvents like MeCN, THF and DMF (Table 6.4, Entry 7-9), with only traces of product detected in DMF. Afterwards, we proceeded to optimize the catalyst loading for the model reaction, with initial catalyst loading of 5 wt% recording 70% yield (Table 6.4, Entry 4). Subsequently, a catalyst loading of 7.5 wt% was sufficient for effective reduction of benzaldehyde to benzylic alcohol with 90% productivity. Upon increasing the catalyst loading from 7.5 wt% to 10 wt%, there was no further change in the productivity of the model reaction. Upon emulating the model reaction under neat conditions, no significant results were observed indicating the necessity of alcoholic solvent and catalyst to complete the reaction (Table 6.4, Entry 12, 13). We further carried out control experiments using the optimized reaction conditions (Table 6.4, Entry 14-16). Under dark condition, the model reaction did not achieve optimum productivity with only traces of product (Table 6.4, Entry 14), signifying the vital role of photoconditions to facilitate the reaction. The model reaction also performed inefficiently in the presence of free radical

scavenger TEMPO, which once again pointed towards generation of free radical species in formation of the reduced product (Table 6.4, Entry 15). Next, when the model reaction was conducted in presence of 7.5 wt% bare oxy-g-CND as the catalyst, the reaction delivered only 40% yield, with the catalyst forming a lump in the reaction medium due to moisture absorption in alcoholic solvent (Table 6.4, Entry 16). Moreover, as discussed earlier, separation and recovery of highly water dispersible oxy-g-CND became a tedious issue. In hindsight, this result indicated that the combination of oxy-g-CND with HPU not only enhanced the productivity of the protocol but also provided heterogeneity for easy and simple catalyst separation.

Table 6.4. Optimization of reaction conditions*a* for reduction of benzaldehyde

Entry	Catalyst (wt%)	Solvent	Time (h)	Yield*b* (%)
1	5.0	H_2O	5	NR#
2	5.0	MeOH	4	50
3	5.0	EtOH	3	60
4	5.0	*i*PrOH	3	70
5	5.0	PhMe	3	NR#
6	5.0	$CHCl_3$	3	NR#
7	5.0	MeCN	3	NR#
8	5.0	THF	3	NR#
9	5.0	DMF	3	Trace
10	7.5	*i*PrOH	3	90
11	10.0	*i*PrOH	3	90
12	-	*i*PrOH	3	NR#
13	10.0	-	3	NR#
14*c*	10.0	*i*PrOH	12	Trace
15*d*	10.0	*i*PrOH	3	Trace
16*e*	10.0	*i*PrOH	3	40

*a*Reaction conditions: Benzaldehyde (1 mmol, 0.106 g), HPUNC catalyst (in wt% with respect to substrate), solvent (3 mL). *b*Isolated product, confirmed by TLC using authentic substrate. *c*Under dark condition. *d*In presence of TEMPO. *e*oxy-g-CND used as catalyst. #No reaction.

After optimization of the reaction conditions, we tried to extend the scope of the HPUNC-photocatalyzed reduction protocol towards various substituted benzaldehyde derivatives. As illustrated in **Table 6.5**, HPUNC photocatalyst was successfully applied for reduction of benzaldehyde derivatives, furnishing the corresponding products in good to high yields (Table 6.5, Entry 2a-2e). The yield of the products were observed to be influenced by different electronic substituents on the substrate, with higher productivity seen in reactants with electron releasing substituents than that of electron withdrawing substituents. The present reaction condition failed to apply to aliphatic isovaleraldehyde (Table 6.5, Entry 2f) and heteryl thiophene-2-carboxaldehyde (Table 6.5, Entry 2g). Thus, the ambit of the metal-free heterogeneous HPUNC photocatalyst was fruitfully applicable to reduction of benzaldehydes derivatives only.
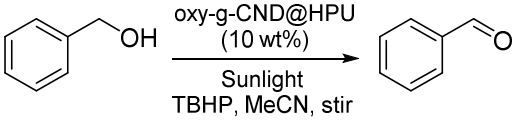
Table 6.5. Substrate study for reduction of benzaldehydes
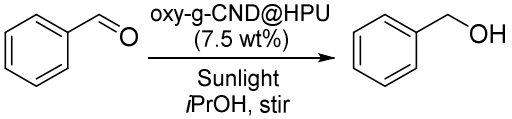
Entry	Reactant	Product	Yield[b] (%)
2a			90
2b			95
2c			95
2d			78
2e			78
2f			NR#
2g			NR#

[a]Reaction conditions: Benzaldehyde derivative (1 mmol, 0.106 g), *i*PrOH (3 mL), HPUNC catalyst (7.5 wt%), under sunlight, 3 h. [b]Isolated product, purified by column chromatography and identified by ^{1}H-NMR analyses (Page 6-38–6-40). #No reaction.

Under the umbrella of green chemistry, recyclability is an important aspect of catalysis. Hence, the recycling potency of the HPUNC photocatalyst was tested using both the model reactions under their respective optimized conditions, as depicted in **Table 6.6**.

Table 6.6. Recyclability of HPUNC photocatalyst

Entry	oxy-g-CND@HPU (10 wt%) Sunlight TBHP, MeCN, stir		
	Cycle	**Time**	**Yield**
1	Fresh	3	95
2	1st	3	92
3	2nd	3	90
4	3rd	3.5	90
5	4th	4	80
	oxy-g-CND@HPU (7.5 wt%) Sunlight *i*PrOH, stir		
	Cycle	**Time**	**Yield**
6	Fresh	3	90
7	1st	3	90
8	2nd	3	90
9	3rd	3	90
10	4th	3	90
11	5th	3	90
12	6th	3	85
13	7th	3	85

In case of the oxidation reaction, HPUNC could be recycled upto 3rd cycle without any significant loss of activity, delivering almost comparable yields (Table 6.6, Entry 1-4). However, a slightly longer reaction time was required during 3rd cycle to achieve near the optimum productivity, as the thin films of photocatalyst aggregated together during the course of the reaction. Moreover, slight discoloration of the photocatalyst was also observed after 3rd cycle probably caused by the action of the oxidant. The activity of the photocatalyst slightly decreased after the 4th cycle, as the thin films stuck together during the reaction (Table 6.6, Entry 5). FT-IR analysis of the fresh catalyst and recovered spent catalyst after 4th cycle displayed very little changes, ensuing the stability of the catalyst.

(**Figure 6.10.a**) TEM images of the recovered catalyst displayed aggregation of the oxy-g-CND within the polymer matrix (**Figure 6.10.b**). In case of the reduction reaction, HPUNC could be easily recycled upto 5th cycle without any loss in its efficiency (Table 6.6, Entry 6-11). Even after 7th cycle, the activity of the photocatalyst showed comparative efficiency (Table 6.6, Entry 12-13), even though photocatalyst appeared discolored possibly due to the adherence of substrate molecules during the course of the reaction. FT-IR spectral analysis of the fresh catalyst and recovered spent catalyst after 7th cycle displayed a near similar pattern with very little changes, signifying its efficiency and stability (**Figure 6.10.a**).
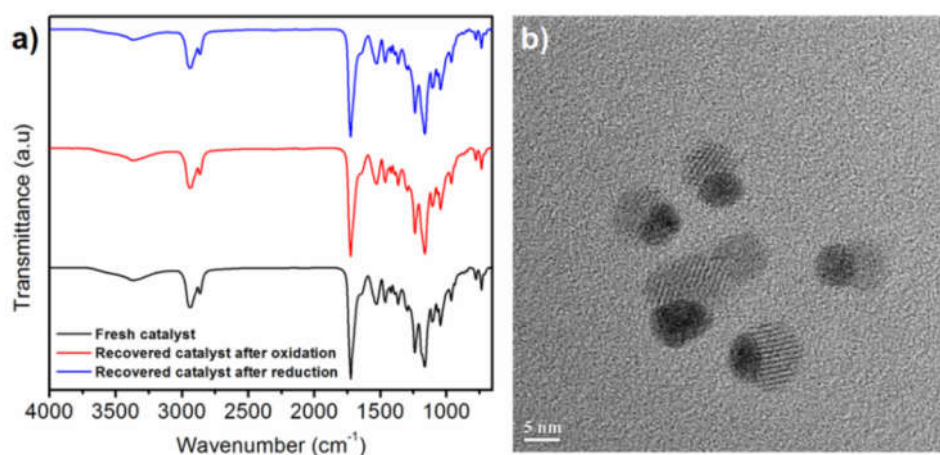
Figure 6.10. a) FT-IR spectra of fresh catalyst and recovered spent catalyst after oxidation reaction and reduction reaction, and **b)** TEM image of recovered catalyst at magnification of 5 nm.

The role of the HPU matrix as a support in the catalyst was investigated by BET surface area analysis. BET surface area analyses of HPU and HPUNC at −195 °C temperature by N_2 physisorption revealed interesting information about the textural nature of HPU matrix. The N_2 adsorption-desorption isotherm of pure HPU (**Figure 6.11.a**) was similar to that of HPUNC (**Figure 6.11.b**), which can be attributed to the comprehensive presence of HPU matrix in both. Both the N_2 adsorption-desorption isotherms closely resembled type IV isotherm with a H2 hysteresis loop, typical of mesoporous materials. Further analysis by BET method divulged a surface area of 121.07 $m^2 g^{-1}$ for HPU and a surface area of 164.871 $m^2 g^{-1}$ for HPUNC. Additionally, pore size distribution estimated by Barrett-Joyner-Halenda (BJH) method revealed a pore volume of 0.016 $cm^3 g^{-1}$ and pore diameter within 3.5-7 nm in pure HPU (Figure 6.10.a, inset), as compared to the pore volume of 0.240 $cm^3 g^{-1}$ and pore diameter range of 3.2-6 nm in HPUNC (Figure 6.10.b, inset). This increase in surface area and decrease in pore volume and pore diameter of the HPUNC compared to pure HPU

can be solely attributed to the presence of oxy-g-CND in the HPU matrix. The oxy-g-CNDs occupied the cavities/pores in the HPU matrix, thereby increasing the surface area of the matrix and decreasing the pore size. These results pointed towards mesoporous nature of the HPU and HPUNC, arising from its three-dimensional architecture with inherent cavities/pores in its structure and explain its efficiency as a support in current catalytic performances. Notably, there may be some contribution of the photothermal effect of sunlight during the overall processes, even after proper thermostating measures, as no light filter was used.
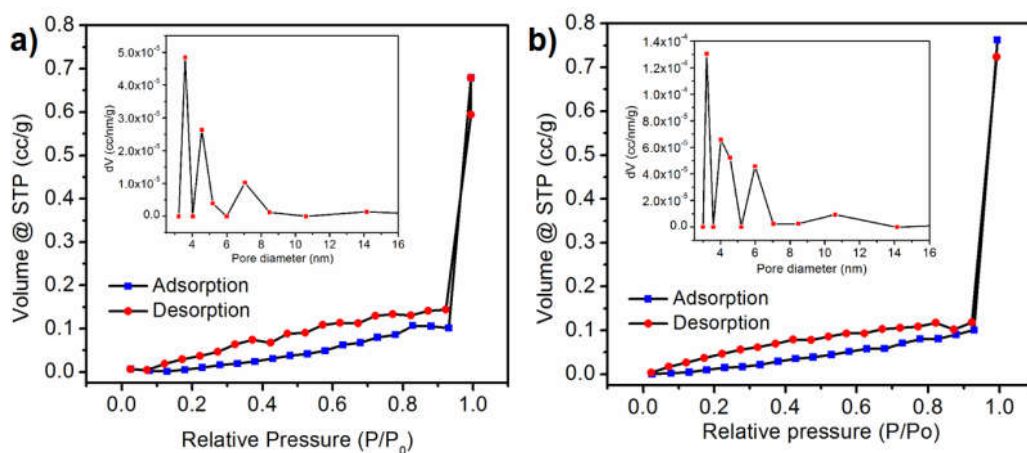
Figure 6.11. N$_2$ adsorption-desorption isotherms of **a)** HPU (inset: Pore size distribution in HPU), and **b)** HPUNC (inset: Pore size distribution in HPUNC).

In general, the reactions were found to be mostly clean and selective, using HPUNC as a heterogeneous metal-free photocatalyst and sunlight as the photo source (**Scheme 6.3**). Here, oxy-g-CNDs served as the photo-active component of the catalytic system that induced photo-redox processes to drive the reaction, while HPU provides the vital mechanical support and bring about selectivity in the reactions through its unique hyperbranched architectural features. The mechanism of both the reactions is still under scrutiny. However, based on the results of control experiments, a free radical mechanism is the most likely pathway. In HPUNC photocatalyst, oxy-g-CNDs act as an electron reservoir, which release photo-induced electrons from the conduction band, generating charge carriers or electron/hole (e$^-$/h$^+$) pairs. These photo-generated e$^-$/h$^+$ pairs interact with the aromatic substrates to form highly reactive transient species. These transient species undergo reaction with oxidative *t*BuOO$^{\cdot}$/*t*BuO$^{\cdot}$/OH$^{\cdot}$ radicals generated from TBHP in case of oxidation process (Pathway A); and with reductive H$^+$ donors from alcoholic solvent in case of reduction process (Pathway B), to yield their corresponding products, as seen in earlier reports [23-25, 47-50]. These oxy-g-CNDs are ably supported by the HPU matrix in

the photocatalytic system. HPU, with its large number of surface functional moieties like –NH–C(=O)–O–, –O–C=O, –OH, –NH, etc. provide the requisite mechanical stability to the oxy-g-CNDs and their unique mesoporous structure act as binding sites for reactants, possibly accounting for the selectivity of products.
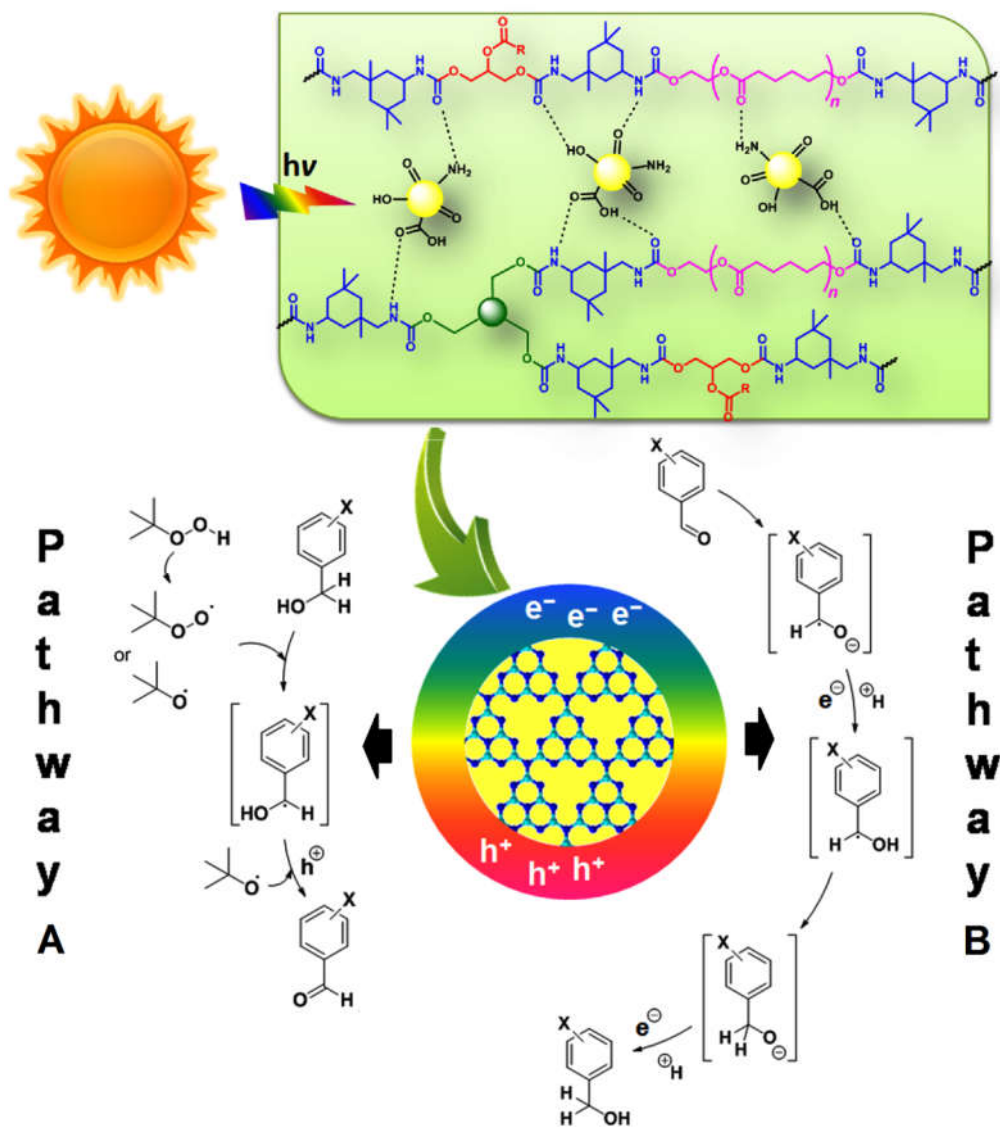

**Scheme 6.3.** Possible pathways of oxy-g-CND@HPU nanocomposite as a heterogeneous photocatalyst under solar light.

6.4. Conclusion

The current chapter describes the aptness of oxygeneous-graphitic-carbon nitride nanodot as a nano-reinforcing agent for *in situ* fabrication of HPUNC. The incorporation of oxygeneous-graphitic-carbon nitride nanodot in the HPU matrix improved the mechanical

and thermal properties of the nanocomposite. Oxygeneous-graphitic-carbon nitride, by the virtue of its characteristic features imparted fascinating optical properties to the nanocomposite. The nanocomposite dispersion exhibited multi-colored photoluminescence under different wavelengths of light, which can be used to design advanced security mark and ink for anti-counterfeiting and covert applications. Alternatively, the nanocomposite films performed well as a robust, efficient and sustainable heterogeneous metal-free photocatalyst for two reverse organic transformations, i.e. oxidation of benzylic alcohols to benzaldehydes and reduction of benzaldehydes to benzylic alcohols, under direct sunlight as the photo source. In overall, the study exemplified HPU/ oxygeneous-graphitic-carbon nitride dot nanocomposite as a high performance material with profound optical and photocatalytic activity.

NMR spectral data of the products of Table 6.3 & Table 6.5

Benzaldehyde (Table 6.3, Entry 1a)
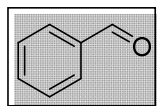
^{1}H NMR (400 MHz, Chloroform-D) δ 9.92 (s, 1H), 7.78 (d, *J* = 8 Hz, 2H), 7.47 (m, 3H).

4-methylbenzaldehyde (Table 6.3, Entry 1b)
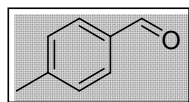
^{1}H NMR (400 MHz, Chloroform-D) δ 9.93 (s, 1H), 7.74 (d, *J* = 8 Hz, 2H), 7.29 (d, *J* = 8 Hz, 2H), 2.40 (s, 3H).

4-methoxybenzaldehyde (Table 6.3, Entry 1c)
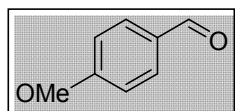
^{1}H NMR (400 MHz, Chloroform-D) δ 9.76 (s, 1H), 7.72 (d, *J* = 8 Hz, 2H), 6.89 (d, *J* = 8 Hz, 2H), 3.76 (s, 3H).

4-bromobenzaldehyde (Table 6.3, Entry 1d)
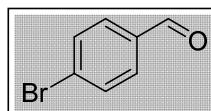
^{1}H NMR (400 MHz, Chloroform-D) δ 9.97 (s, 1H), 7.71 (m, 4H).

4-nitrobenzaldehyde (Table 6.3, Entry 1e)
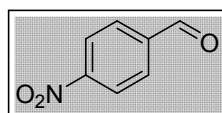
^{1}H NMR (400 MHz, Chloroform-D) δ 10.15 (s, 1H), 8.38 (d, *J* = 8.0 Hz, 2H), 8.06 (d, *J* = 8.0 Hz, 2H).

Benzyl alcohol (Table 6.5, Entry 2a)
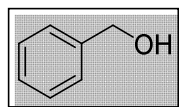
^{1}H NMR (400 MHz, Chloroform-D) δ 7.55 – 7.22 (m, 5H), 4.60 (s, 2H), 2.83 (s, 1H).

4-methylbenzyl alcohol (Table 6.5, Entry 2b)
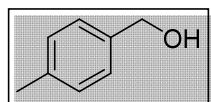
^{1}H NMR (400 MHz, Chloroform-D) δ 7.20 (dd, *J* = 30.9, 8.0 Hz, 4H), 4.61 (s, 2H), 2.35 (s, 3H), 2.00 (s, 1H).
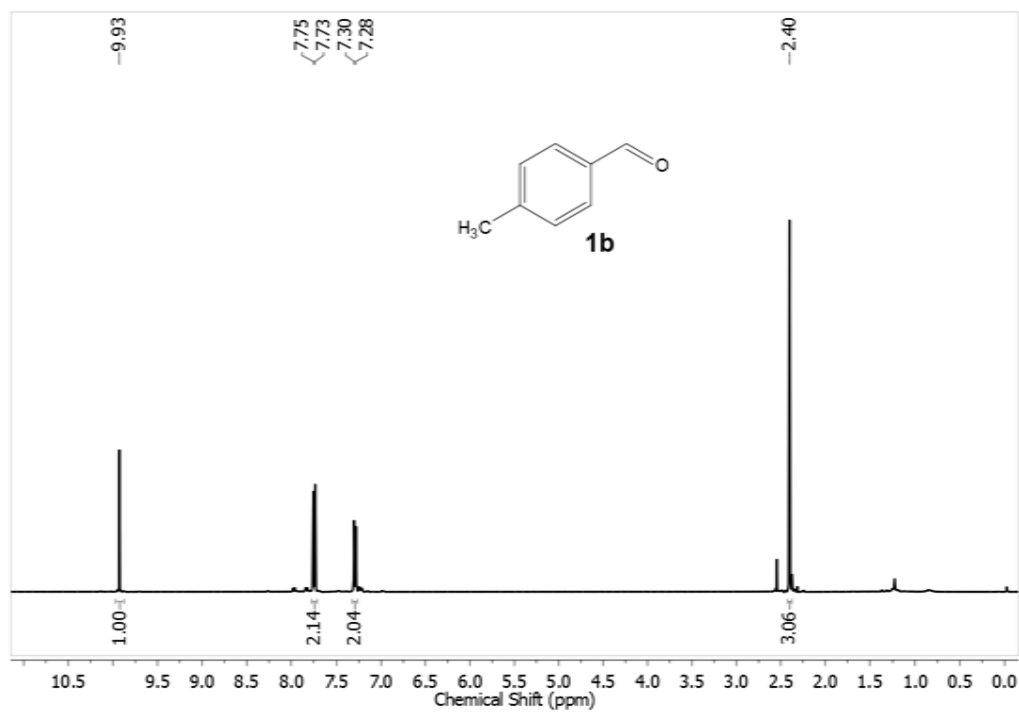
4-methoxybenzyl alcohol (Table 6.5, Entry 2c)
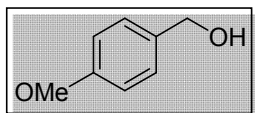
^{1}H NMR (400 MHz, Chloroform-D) δ 7.22 (d, J = 8.0 Hz, 2H), 6.85 (d, J = 8.0 Hz, 2H), 4.51 (d, J = 6.2 Hz, 2H), 3.76 (s, 3H), 2.65 (s, 1H).
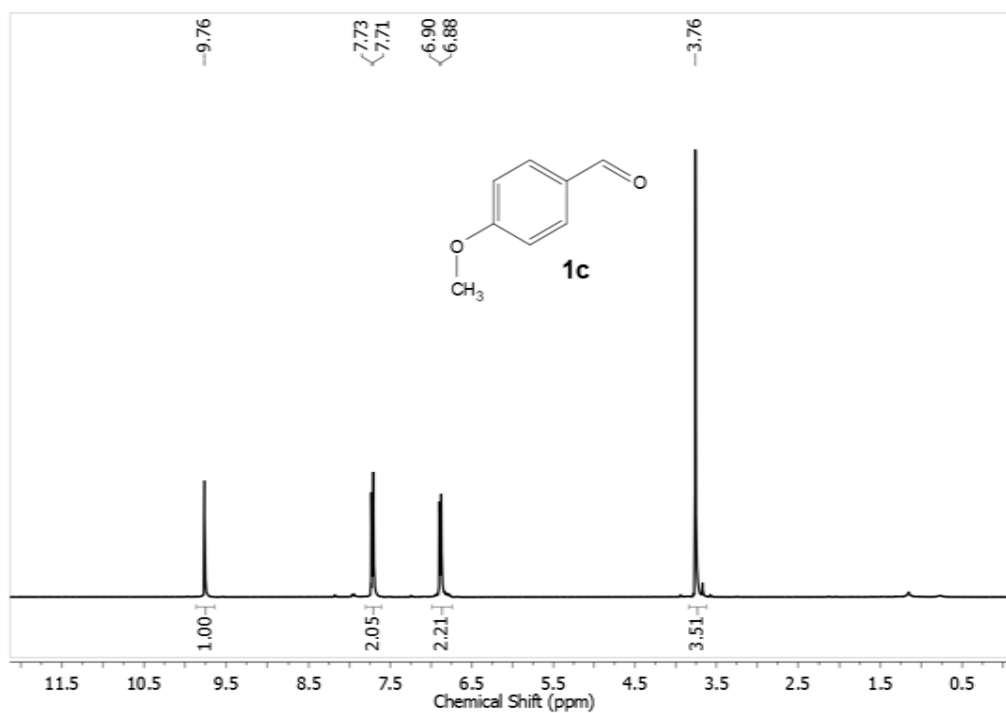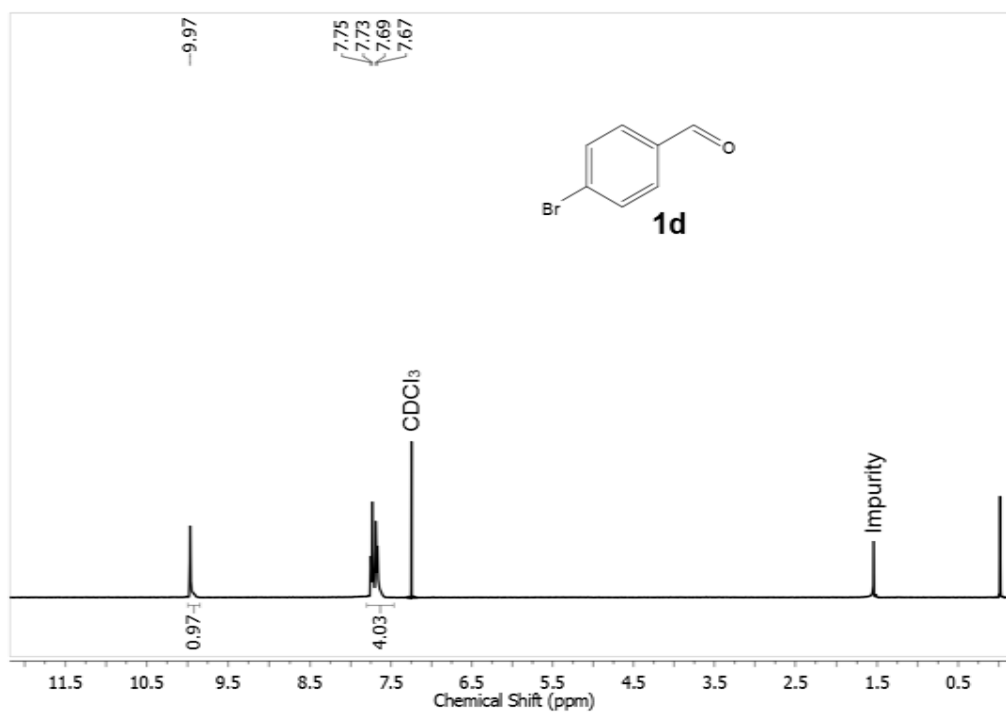
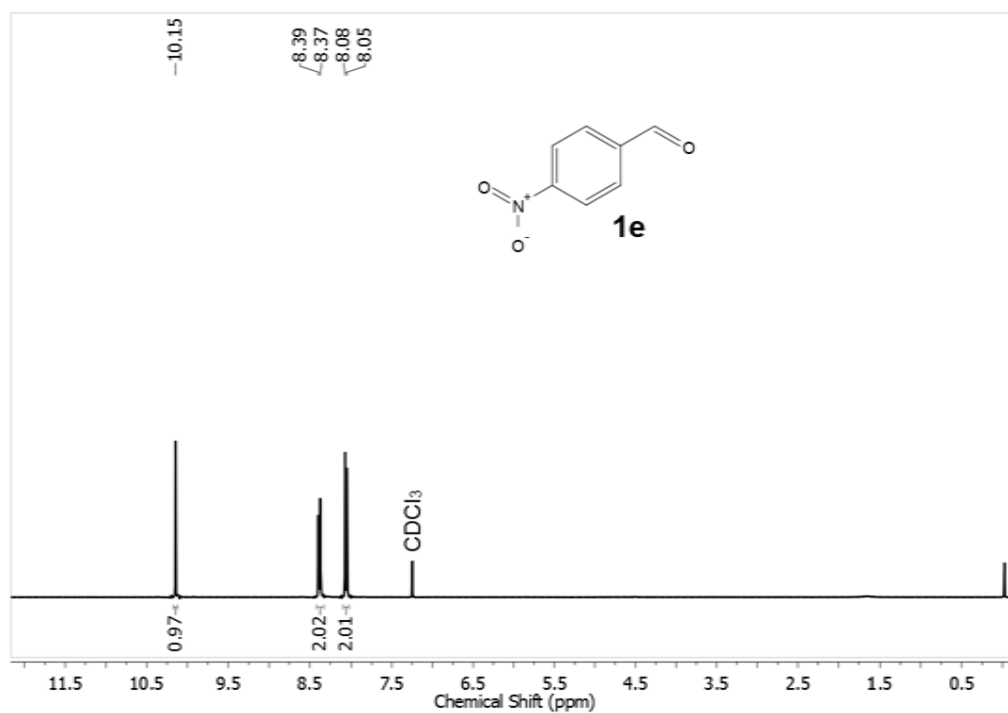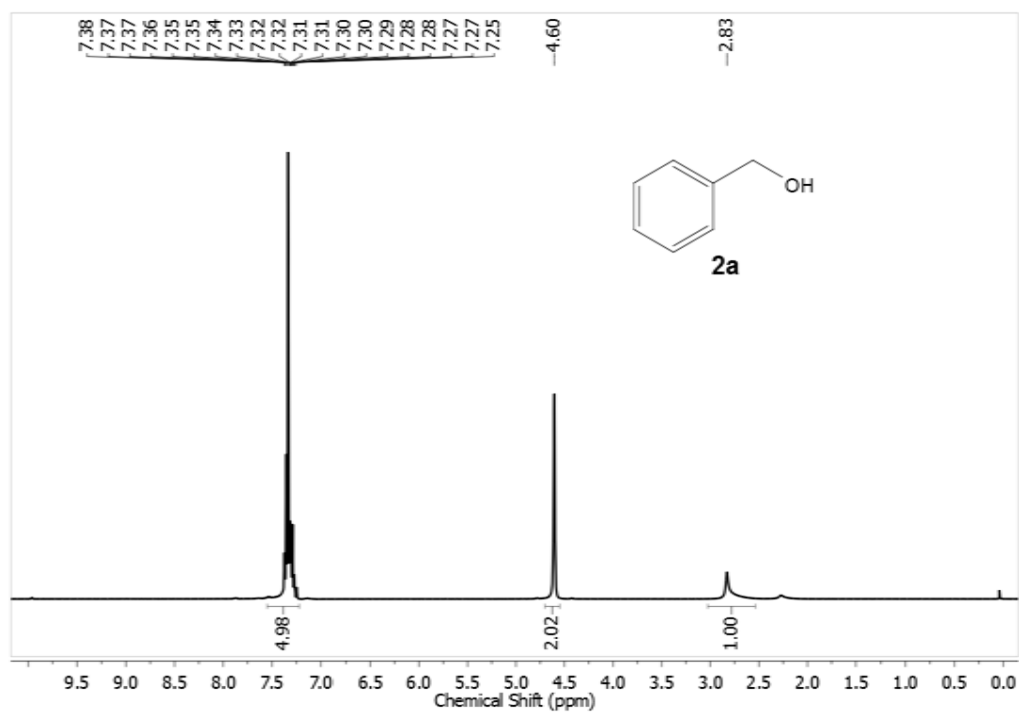### 4-nitrobenzyl alcohol (Table 6.5, Entry 2d)
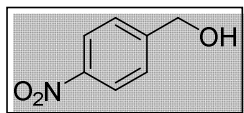
^{1}H NMR (400 MHz, Chloroform-D) δ 8.18 (d, J = 8 Hz, 2H), 7.51 (d, J = 8 Hz, 2H), 4.82 (s, 2H), 2.19 (s, 1H).
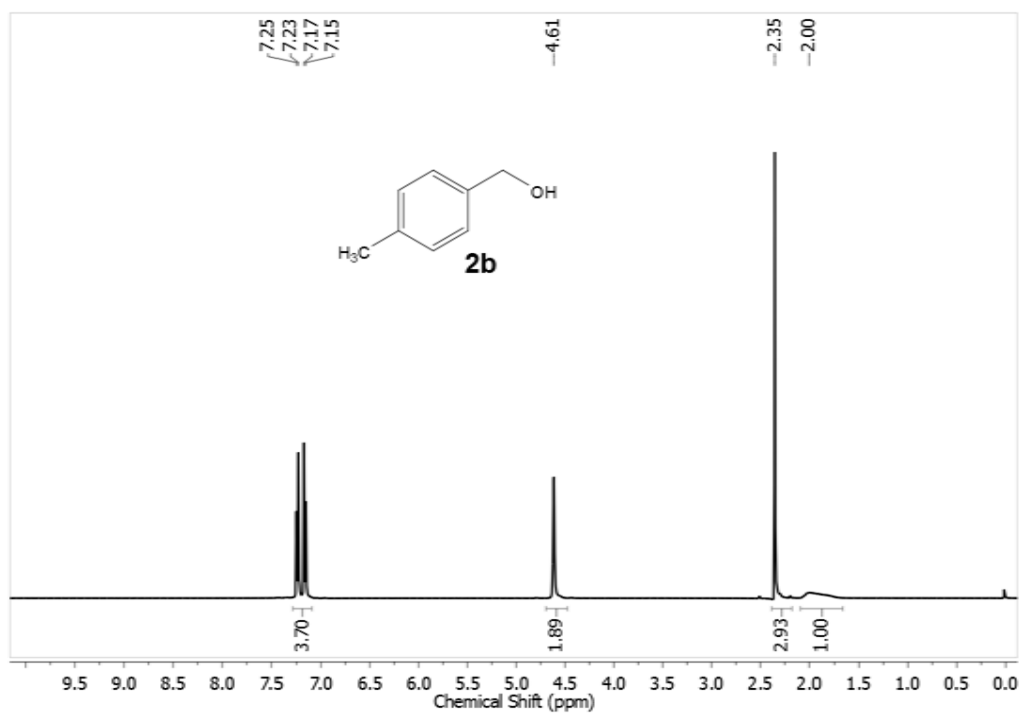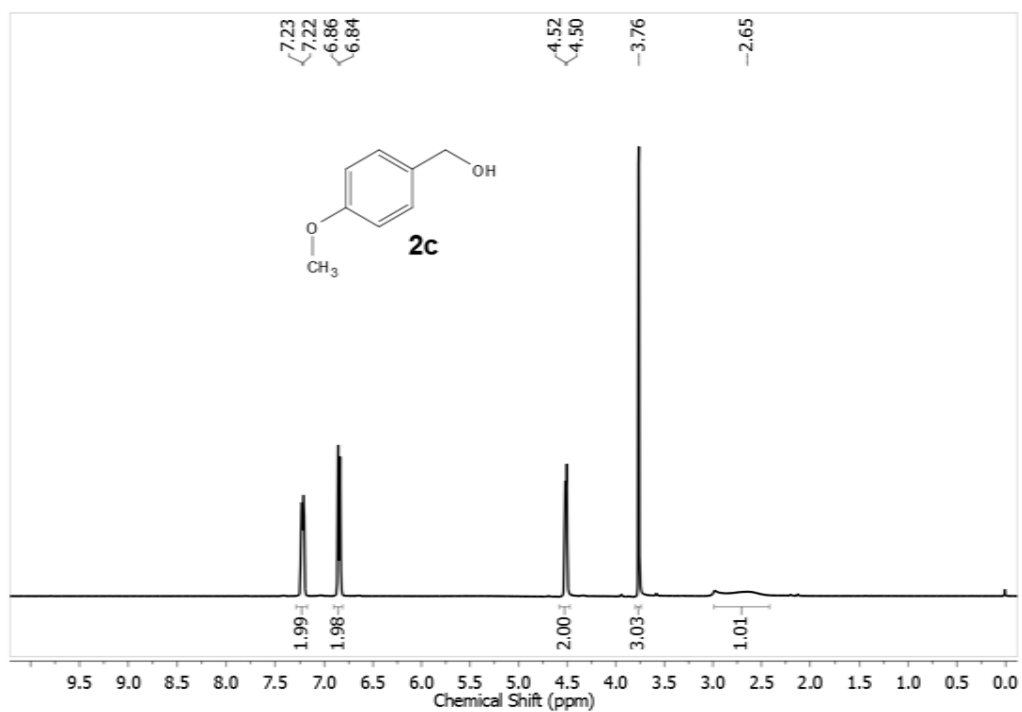
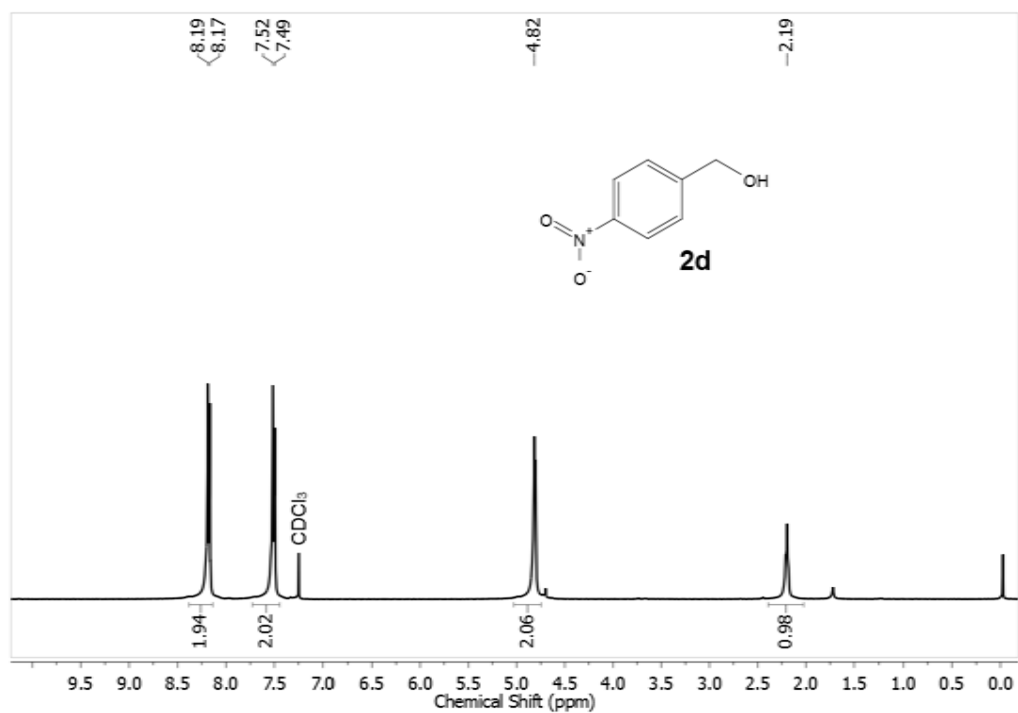### 4-fluorobenzyl alcohol (Table 6.5, Entry 2e)
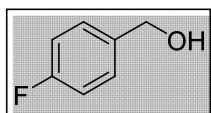
^{1}H NMR (400 MHz, Chloroform-D) δ 7.24 (d, J = 8 Hz, 2H), 6.98 (t, J = 8 Hz, 2H), 4.51 (s, 2H), 3.35 (s, 1H).

¹H NMR spectrum of Benzaldehyde (Table 6.3, Entry 1a):
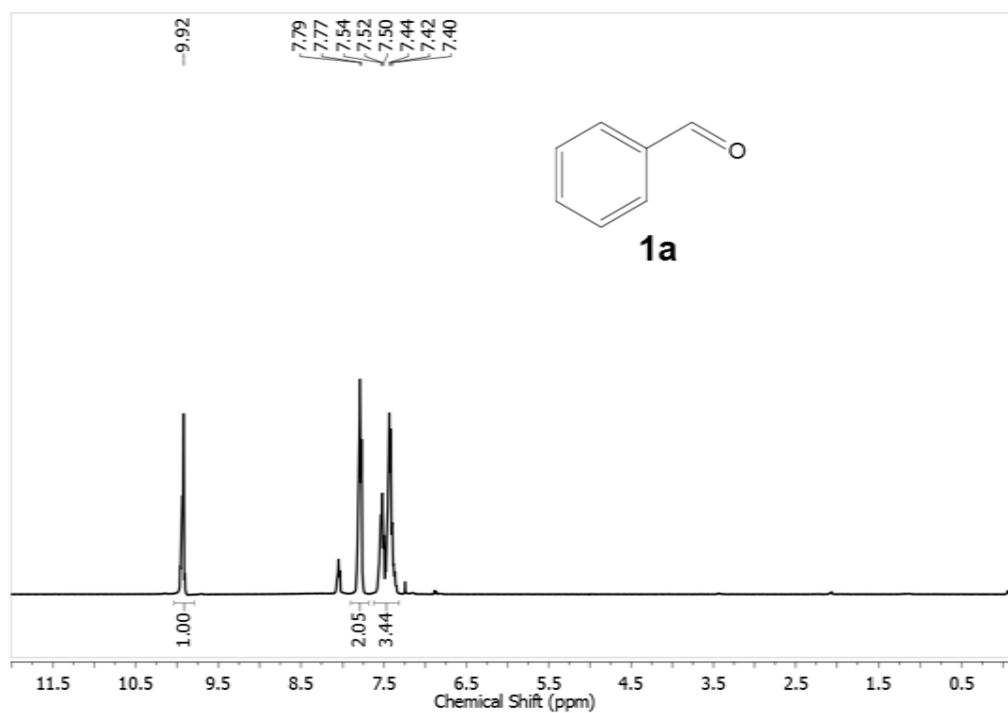
¹H NMR spectrum of 4-methylbenzaldehyde (Table 6.3, Entry 1b):

¹H NMR spectrum of 4-methoxybenzaldehyde (Table 6.3, Entry 1c):

¹H NMR spectrum of 4-bromobenzaldehyde (Table 6.3, Entry 1d):

¹H NMR spectrum of 4-nitrobenzaldehyde (Table 6.3, Entry 1e):

¹H NMR spectrum of Benzyl alcohol (Table 6.5, Entry 2a):

¹H NMR spectrum of 4-methylbenzyl alcohol (Table 6.5, Entry 2b):

¹H NMR spectrum of 4-methoxybenzyl alcohol (Table 6.5, Entry 2c):

¹H NMR spectrum of 4-nitrobenzyl alcohol (Table 6.5, Entry 2d):

¹H NMR spectrum of 4-fluorobenzyl alcohol (Table 6.5, Entry 2e):
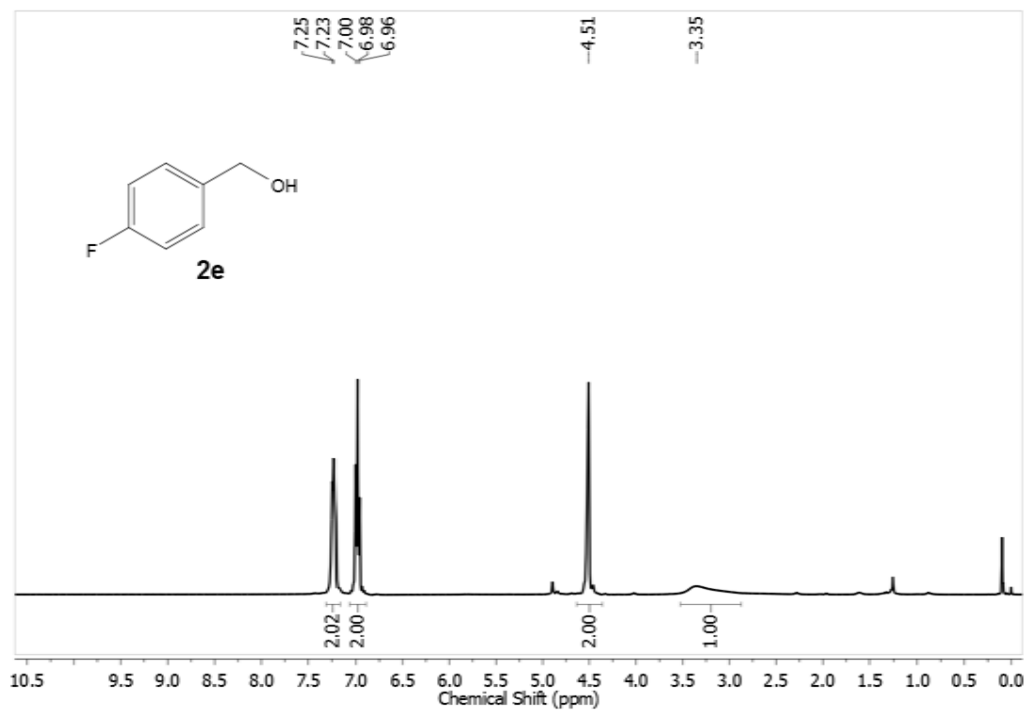
References

[1]   Zhu, J., Xiao, P., Li, H., and Carabineiro, S. A. Graphitic carbon nitride: synthesis, properties, and applications in catalysis. *ACS Applied Materials & Interfaces*, 6(19):16449-16465, 2014.

[2]   Zhao, Z., Sun, Y., and Dong, F. Graphitic carbon nitride based nanocomposites: A review. *Nanoscale*, 7(1):15-37, 2015.

[3]   Ong, W. J., Tan, L. L., Ng, Y. H., Yong, S. T., and Chai, S. P. Graphitic carbon nitride (g-C_3N_4)-based photocatalysts for artificial photosynthesis and environmental remediation: are we a step closer to achieving sustainability? *Chemical Reviews*, 116(12):7159-7329, 2016.

[4]   Wang, Y., Wang, X., and Antonietti, M. Polymeric graphitic carbon nitride as a heterogeneous organocatalyst: from photochemistry to multipurpose catalysis to sustainable chemistry. *Angewandte Chemie International Edition*, 51(1):68-89, 2012.

[5]   Lu, L., Lv, Z., Si, Y., Liu, M., and Zhang, S. Recent progress on band and surface engineering of graphitic carbon nitride for artificial photosynthesis. *Applied Surface Science*, 462:693-712, 2018.

[6]   Zhu, L., You, L., Shi, Z., Song, H., and Li, S. An investigation on the graphitic carbon nitride reinforced polyimide composite and evaluation of its tribological properties. *Journal of Applied Polymer Science*, 134(41):45403, 2017.

[7]   Xu, J. H., Ye, S., Di Ding, C., Tan, L. H., and Fu, J. J. Autonomous self-healing supramolecular elastomer reinforced and toughened by graphitic carbon nitride nanosheets tailored for smart anticorrosion coating applications. *Journal of Materials Chemistry A*, 6(14):5887-5898, 2018.

[8]   Yoon, B., Lee, J., Park, I. S., Jeon, S., Lee, J., and Kim, J. M. Recent functional material based approaches to prevent and detect counterfeiting. *Journal of Materials Chemistry C*, 1(13):2388-2403, 2013.

[9]   Hardwick, B., Jackson, W., Wilson, G., and Mau, A. W. Advanced materials for banknote applications. *Advanced Materials*, 13(12-13):980-984, 2001.

[10] Prime, E. L. and Solomon, D. H. Australia's plastic banknotes: fighting counterfeit currency. *Angewandte Chemie International Edition*, 49(22):3726-3736, 2010.

[11] Deisingh, A. K. Pharmaceutical counterfeiting. *Analyst*, 130(3):271-279, 2005.

[12] Aldhous, P. Counterfeit pharmaceuticals: murder by medicine. *Nature*, 434:132, 2005.

[13]   Kennedy, Z. C., Stephenson, D. E., Christ, J. F., Pope, T. R., Arey, B. W., Barrett, C. A., and Warner, M. G. Enhanced anti-counterfeiting measures for additive manufacturing: coupling lanthanide nanomaterial chemical signatures with blockchain technology. *Journal of Materials Chemistry C*, 5(37):9570-9578, 2017.

[14]   Kumar, P., Singh, S., and Gupta, B. K. Future prospects of luminescent nanomaterial based security inks: from synthesis to anti-counterfeiting applications. *Nanoscale*, 8(30):14297-14340, 2018.

[15]   Jiang, K., Zhang, L., Lu, J., Xu, C., Cai, C., and Lin, H. Triple-mode emission of carbon dots: applications for advanced anti-counterfeiting. *Angewandte Chemie International Edition*, 55(25):7231-7235, 2016.

[16]   Ravelli, D., Dondi, D., Fagnoni, M., and Albini, A. Photocatalysis. A multi-faceted concept for green chemistry. *Chemical Society Reviews*, 38(7):1999-2011, 2009.

[17]   Wang, X., Wang, F., Sang, Y., and Liu, H. Full-spectrum solar-light-activated photocatalysts for light–chemical energy conversion. *Advanced Energy Materials*, 7(23):1700473, 2017.

[18]   Yu, Y., Yan, W., Gao, W., Li, P., Wang, X., Wu, S., Song, W., and Ding, K. Aromatic ring substituted g-C_3N_4 for enhanced photocatalytic hydrogen evolution. *Journal of Materials Chemistry A*, 5(33):17199-17203, 2017.

[19]   Gao, Y., Hou, F., Hu, S., Wu, B., and Jiang, B. Synchronization iodine surface modification and lattice doping porous carbon nitride for photocatalytic hydrogen production. *Applied Surface Science*, 481:1089-1095, 2019.

[20]   Alam, K. M., Kumar, P., Kar, P., Thakur, U. K., Zeng, S., Cui, K., and Shankar, K. Enhanced charge separation in g-C_3N_4–BiOI heterostructures for visible light driven photoelectrochemical water splitting. *Nanoscale Advances*, 1(4):1460-1471, 2019.

[21]   Yao, C., Yuan, A., Wang, Z., Lei, H., Zhang, L., Guo, L., and Dong, X. Amphiphilic two-dimensional graphitic carbon nitride nanosheets for visible-light-driven phase-boundary photocatalysis. *Journal of Materials Chemistry A*, 7(21):13071-13079, 2019.

[22]   Su, F., Mathew, S. C., Lipner, G., Fu, X., Antonietti, M., Blechert, S., and Wang, X. mpg-C_3N_4-catalyzed selective oxidation of alcohols using O_2 and visible light. *Journal of American Chemical Society*, 132(46):16299-16301, 2010.

[23]   Wang, Y., Li, H., Yao, J., Wang, X., and Antonietti, M. Synthesis of boron doped polymeric carbon nitride solids and their use as metal-free catalysts for aliphatic C–H bond oxidation. *Chemical Science*, 2(3):446-450, 2011.

[24] Chen, Y., Zhang, J., Zhang, M., and Wang, X. Molecular and textural engineering of conjugated carbon nitride catalysts for selective oxidation of alcohols with visible light. *Chemical Science*, 4(8):3244-3248, 2013.

[25] Long, B., Ding, Z., and Wang, X. Carbon nitride for the selective oxidation of aromatic alcohols in water under visible light. *ChemSusChem*, 6(11):2074-2078, 2013.

[26] Zhou, M., Yang, P., Yuan, R., Asiri, A. M., Wakeel, M., and Wang, X. Modulating crystallinity of graphitic carbon nitride for photocatalytic oxidation of alcohols. *ChemSusChem*, 10(22):4451-4456, 2017.

[27] Cerdan, K., Ouyang, W., Colmenares, J. C., Muñoz-Batista, M. J., Luque, R., and Balu, A. M. Facile mechanochemical modification of g-C_3N_4 for selective photo-oxidation of benzyl alcohol. *Chemical Engineering Science*, 194:78-84, 2019.

[28] Caminade, M., Yan, D., and Smith, D. K. Dendrimers and hyperbranched polymers. *Chemical Society Reviews*, 44(12):3870-3873, 2015.

[29] Astruc, D. and Chardac, F. Dendritic catalysts and dendrimers in catalysis. *Chemical Reviews*, 101(9):2991-3024, 2001.

[30] Gogoi, S. and Karak, N. Solar-driven hydrogen peroxide production using polymer-supported carbon dots as heterogeneous catalyst. *Nano-Micro Letters*, 9(4):40, 2017.

[31] Das, V. K., Gogoi, S., Choudary, B. M., and Karak, N. A promising catalyst for exclusive *para* hydroxylation of substituted aromatic hydrocarbons under UV light. *Green Chemistry*, 19(18):4278-4283, 2017.

[32] Anselme, J. P. Understanding oxidation-reduction in organic chemistry. *Journal of Chemical Education*, 74(1):69-72, 1997.

[33] March, J. *Advanced Organic Chemistry: Reactions, Mechanisms and Structure*, John Wiley & Sons, Hoboken, 4th edition, 2007.

[34] Carruthers, W. and Coldham, I. *Modern Methods of Organic Synthesis*, Cambridge University Press, Cambridge, 4th edition, 2004.

[35] Tang, Y., Su, Y., Yang, N., Zhang, L., and Lv, Y. Carbon nitride quantum dots: A novel chemiluminescence system for selective detection of free chlorine in water. *Analytical Chemistry*, 86(9):4528-4535, 2014.

[36] Zhou, J., Yang, Y., and Zhang, C. Y. A low-temperature solid-phase method to synthesize highly fluorescent carbon nitride dots with tunable emission. *Chemical Communications*, 49(77):8605-8607, 2013.

[37] Schwenke, A. M., Hoeppener, S., and Schubert, U. S. Synthesis and modification of carbon nanomaterials utilizing microwave heating. *Advanced Materials*, 27(28):4113-4141, 2015.

[38]   Li, X., Zhang, J., Shen, L., Ma, Y., Lei, W., Cui, Q., and Zou, G. Preparation and characterization of graphitic carbon nitride through pyrolysis of melamine. *Applied Physics A*, 94(2):387-392, 2009.

[39]   Fan, X., Feng, Y., Su, Y., Zhang, L., and Lv, Y. A green solid-phase method for preparation of carbon nitride quantum dots and their applications in chemiluminescent dopamine sensing. *RSC Advances*, 5(68):55158-55164, 2015.

[40]   Khabashesku, V. N., Zimmerman, J. L., and Margrave, J. L. Powder synthesis and characterization of amorphous carbon nitride. *Chemistry of Materials*, 12(11):3264-3270, 2000.

[41]   Pan, D. Y., Zhang, J. C., Li, Z., Wu, C., Yan, X. M., and Wu, M. H. Observation of pH-, solvent, spin-, and excitation-dependent blue photoluminescence from carbon nanoparticles. *Chemical Communications*, 46(21):3681-3683, 2010.

[42]   Pan, D., Zhang, J., Li, Z., and Wu, M. Hydrothermal route for cutting graphene sheets into blue-luminescent graphene quantum dots. *Advanced Materials*, 22(6):734-738, 2010.

[43]   Ghosh, B., Gogoi, S., Thakur, S., and Karak, N. Bio-based waterborne polyurethane/ carbon dot nanocomposite as a surface coating material. *Progress in Organic Coatings*, 90:324-330, 2016.

[44]   Karak, N., Rana, S., and Cho, J. W. Synthesis and characterization of castor-oil-modified hyperbranched polyurethanes. *Journal of Applied Polymer Science*, 112(2):736-743, 2009.

[45]   Mittal, G., Dhand, V., Rhee, K. Y., Park, S. J., and Lee, W. R. A review on carbon nanotubes and graphene as fillers in reinforced polymer nanocomposites. *Journal of Industrial and Engineering Chemistry*, 21:11-25, 2015.

[46]   Gobi, N., Vijayakumar, D., Keles, O., and Erogbogbo, F. Infusion of graphene quantum dots to create stronger, tougher, and brighter polymer composites. *ACS Omega*, 2(8):4356-4362, 2017.

[47]   Zhang, C., Du, L., Liu, C., Li, Y., Yang, Z., and Cao, Y. C. Photostable epoxy polymerized carbon quantum dots luminescent thin films and the performance study. *Results in Physics*, 6:767-771, 2016.

[48]   De, B., Kumar, M., Mandal, B. B., and Karak, N. An in situ prepared photo-luminescent transparent biocompatible hyperbranched epoxy/carbon dot nanocomposite. *RSC Advances*, 5(91):74692-74704, 2015.

[49]   Hazarika, D. and Karak, N. Biodegradable tough waterborne hyperbranched polyester/carbon dot nanocomposite: approach towards an eco-friendly material. *Green Chemistry*, 18(19):5200-5211, 2016.

[50] Tan, J., Zheng, T., Yu, Y., and Xu, K. TBHP-promoted direct oxidation reaction of benzylic C_{sp3}–H bonds to ketones. *RSC Advances*, 7(25):15176-15180, 2017.

[51] Loeffler, M. J., Fama, M., Baragiola, R. A., and Carlson, R.W. Photolysis of H_2O–H_2O_2 mixtures: The destruction of H_2O_2. *Icarus*, 226(1):945-950, 2013.